ACS Catalysis

pubs.acs.org/acscatalysis Research Article

A Branchpoint Cytochrome P450 CYP512A13 Interconverts Different Types of *Ganoderma* Triterpenoids

Qin Wang, Zeqian Du, Zhenhao Li, Wei Yuan, Jian-Jiang Zhong, Juan Guo, Shenggan Luo, Ting Shi,* and Han Xiao*

Cite This: *ACS Catal.* 2025, 15, 13428−13443 Read Online

ACCESS | Metrics & More | Article Recommendations | Supporting Information

ABSTRACT: The enone is a widely occurring structural unit and functional motif in natural products. Its synthesis at specific positions on the lanostane skeleton represents a hallmark feature of type I ganoderic acids (GAs), a class of triterpenoids from *Ganoderma lucidum*renowned for their potent pharmacological properties. However, the current knowledge on their biosynthesis is limited to the notion that type I GA serves as the direct precursor of type II GAs, another class of bioactive *Ganoderma* triterpenoids. Here, we report a groundbreaking discovery: a multifunctional cytochrome CYP512A13, which directly catalyzes the conversion of the carbon−carbon conjugated double bond on the lanostane skeleton, the hallmark feature of type II GA, into an enone. This transformation is facilitated by a water channel and the C15 hydroxyl group of the substrate, representing an exceptionally rare mechanism in enone biosynthesis. Beyond this remarkable activity, CYP512A13 demonstrates catalytic promiscuity, hydroxylating additional carbon positions on the same substrate to generate unreported type II GAs. By integrating computational modeling with experimental validation, we elucidated the catalytic mechanism of CYP512A13, revealing its dual capability to produce both enone-containing type I GAs and type II GAs. Leveraging these insights, we employed rational design to engineer CYP512A13, achieving selective production of these distinct GA classes. Our findings not only uncover a critical biosynthetic route for the interconversion of GA types but also significantly expand the synthetic biology toolkit, enabling the efficient biosynthesis of high-value *Ganoderma* triterpenoids.

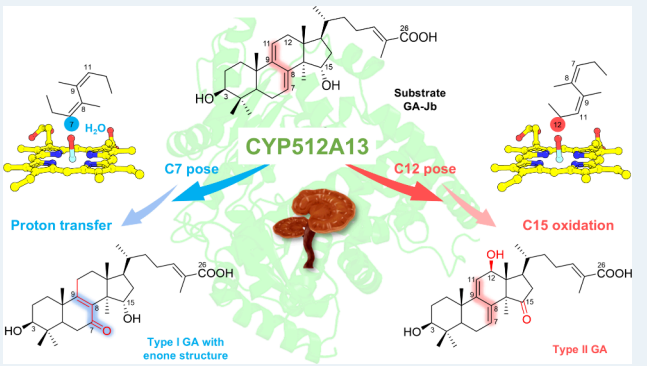

KEYWORDS: *triterpenoids, ganoderic acids (GAs), cytochrome P450 (CYP), enone, synthetic biology*

1. INTRODUCTION

Among the complex triterpenoids identified in the fungi kingdom, ganoderic acids (GAs) derived from the edible and medicinal mushroom *Ganoderma* stand out remarkably, owing to their extensive biological activities.[1] With a lanostane skeleton, GAs can be classified into two types by the positions of the double bonds on the skeleton. Type I GAs possess one double bond at C8 and C9, whereas type II GAs feature a pair of carbon−carbon conjugated double bonds at C7, C8 and C9, C11 (Figure 1A). Among them, type I GAs exhibit remarkable structural diversity and abundance, constituting 75% of the reported *Ganoderma* triterpenoids. Over 80% of type I GAs possess a pair of carbon−oxygen conjugated double bonds at C8, C9 and C7, C8 (or C9, C11) within the tetracyclic ring.[2] This is a crucial functional group prevalently found in pharmaceuticals, agrochemicals, and natural products, namely, the enone (α,β-unsaturated ketone).

As one of the commonly encountered structural units, enone has been documented in compounds such as polyketides, steroids, and terpenoids.[3−5] It is a potent Michael receptor that readily reacts with a diverse range of nucleophilic reagents.[6] For instance, it can covalently bind to the sulfur moiety of cysteine residues within the active sites of target proteins (e.g., protein kinases and transcription factors).[7] This binding event leads to the inhibition of these proteins' activities, which represents a key mechanism underlying their biological effects. As a privileged structural fragment present in various bioactive natural products, including ainsliadimer A, hypothemycin, and helenalin (Figure S1), enone has been reported to target specific cysteine residues in key proteins. Specifically, it targets Cys46 of IKKβ,[8] Cys166 of ERK2,[9] and Cys38 of p65.[10] By interacting with these residues, enone modulates the relevant signaling pathway, thereby inhibiting tumor growth and inflammatory responses. Consequently, enone is widely recognized as a crucial pharmacophore in natural anticancer

Received: June 13, 2025
Revised: July 8, 2025
Accepted: July 9, 2025
Published: July 21, 2025

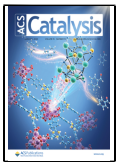

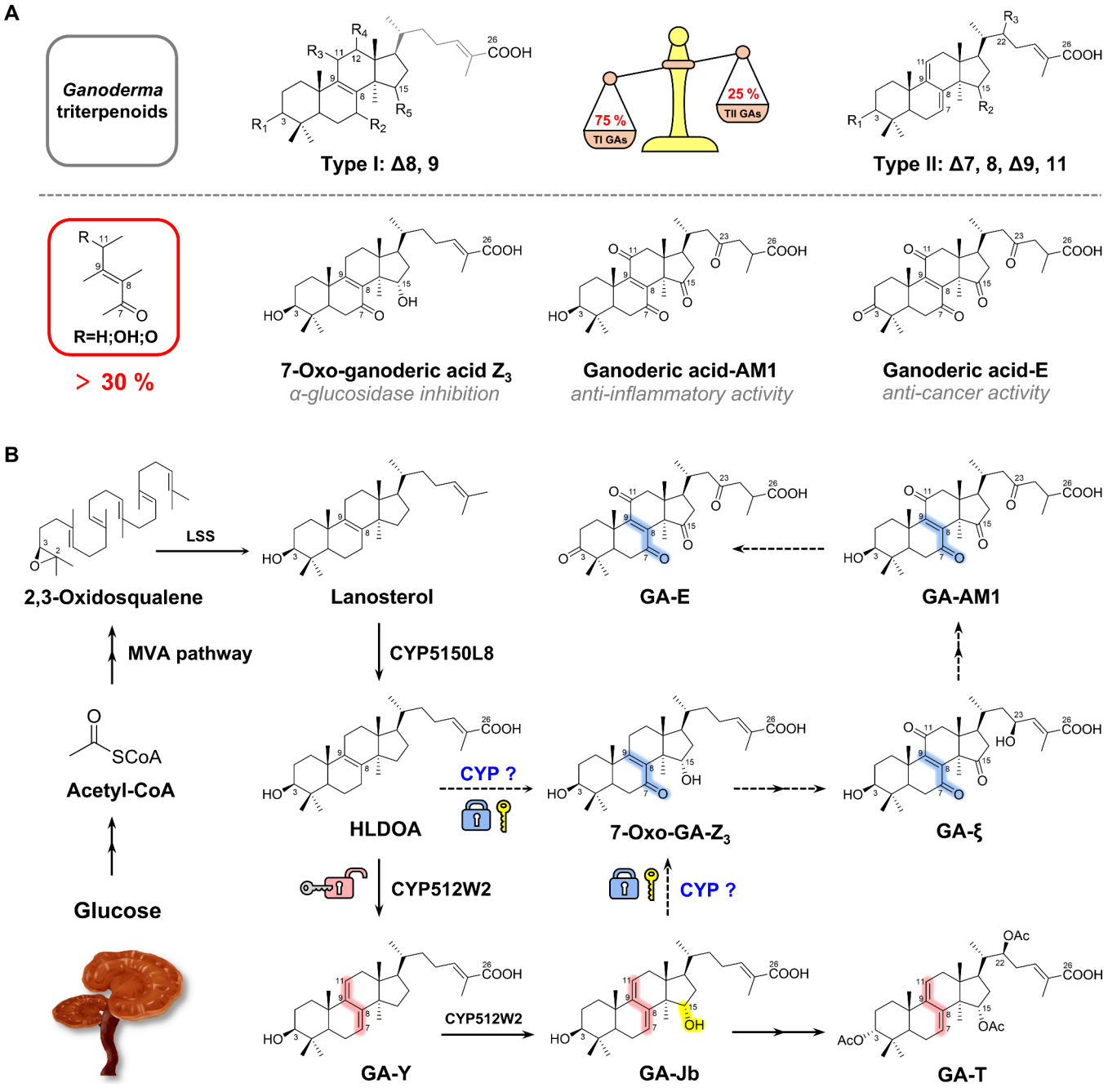

Figure 1. Classification of GAs and the proposed biosynthetic routes. (A) Classification of GAs and their bioactivities. GAs can be group into type I GAs (with a double bond at C8 and C9) and type II GAs (with a pair of carbon−carbon conjugated double bonds at C7, C8 and C9, C11). Side chains (gray) of type I GAs are modified at C20 or C22 or C23, or have a keto group at C23 and single bond at C24 and C25. Type I GAs constitute 75% of total GAs. Over 30% of type I GAs possess a pair of carbon−oxygen conjugated double bonds at C8, C9 and C7, C8 within the tetracyclic ring, namely the enone, and these GAs demonstrate favorable physiological activities. (B) Proposed biosynthetic routes of GAs. After generation of acetyl-CoA from glucose via the central metabolic pathway, 2,3-oxidosqualene is formed via the mevalonate (MVA) pathway and converted into lanosterol by lanosterol synthase (LSS). Two previous characterized CYPs enable the conversion of lanosterol to HLDOA, and to GA-Y and GA-Jb.[18,24] Other enzymes required to form the end type II GAs were characterized in our recent work.[19] CYPs capable of generation of the enone structure remain unknown. The characterized steps and uncharacterized steps are indicated as fulfillment arrows and dashed arrows, respectively. Single step reaction and multistep reactions are indicated as single arrow and double arrows, respectively. The enone structures of type I GAs and the conjugated double bonds of type II GAs are highlighted as blue and red, respectively.

agents. This is evident in FDA-approved drugs such as CDDO-Me[11] and ibrutinib[12] (Figure S1), both of which contain this pharmacophore. Over 30% of type I GAs feature enone structure at C7, C8 and C8, C9, and these GAs demonstrate favorable physiological activities in α-glucosidase inhibition, anti-inflammation, and anticancer (Figure 1A).[13−16] Moreover, five enone-containing type I GAs have advanced to preclinical or clinical trials.[17] Despite the biosynthetic network of type II GAs, another group of bioactive *Ganoderma* triterpenoids,[18] being decoded in our recent work,[19] reports on the biosynthetic pathways for type I GAs remain scarce, particularly regarding the formation of their significant enone

https://doi.org/10.1021/acscatal.5c04095
ACS Catal. 2025, 15, 13428−13443

structure.[20,21] The lack of production routes restricts both the biological exploration and the application of type I GAs.

GAs are biosynthesized from lanosterol in *G. lucidum*.[22] Current understanding of GAs' biosynthesis proposes a three-step oxidation of lanosterol at C26 to form HLDOA, an enone-free type I GA, which serves as the precursor of all downstream GAs[18,23,24] (Figure 1B). Among all the postmodifications, hydroxylation and oxidation are the predominant forms in type I GAs, which implies the participation of cytochrome P450s (CYPs) in their biosynthetic pathways (Figure S2). In addition to successive oxidation at C26, upon careful examination of the chemical structures, we observed that a large part of the characterized type I GA molecules harbor C15 oxidative modification (including hydroxylation, ketonization, and O-acetylation).[2,25] This observation allowed us to infer that C15-oxidized HLDOA might be the precursor of type I GAs (Figure 1B). However, after individually introducing 158 CYPs from *Ganoderma* into the C15 hydroxylated HLDOA producing yeast, none of them were able to generate the enone structure (Figure S2).[18] Thus, unknown enzymes that modify the lanostane skeleton remain, leading to pathway bifurcation between different types of GAs. Our work aims to characterize the enzyme to establish the biosynthetic routes to the characteristic structure of type I GAs.

2. MATERIALS AND METHODS

2.1. Chemicals and Enzymes. HLDOA, 7-oxo-GA-Z_3, GA-Y, GA-Jb, **1**, **2**, and **3** were obtained by extraction and purification of yeast fermentation cultures. NADPH was purchased from Beyotime Biotechnology Co., Ltd. (Shanghai, China). HPLC grade methanol, acetonitrile, and ethyl acetate were purchased from Dikma Technologies (Beijing, China). Other chemicals and reagents were purchased from Sinopharm Chemical Reagent (Shanghai, China) and Sigma-Aldrich (Stanford, MA, USA) unless otherwise specified. All endonucleases used in this study were purchased from New England Biolabs (Ipswich, MA, USA).

2.2. Strains and Cultivation Conditions. *Escherichia coli* DH5α (Tsingke, Beijing, China) was used as a cloning host. *E. coli* strains were grown in Luria−Bertani (LB) media containing 100 mg/L ampicillin at 37 °C and 220 rpm.*G. lucidum*strain CGMCC (China General Microbiological Culture Collection Center, Beijing, China) 5.616 was cultivated for metabolites detection, RNA extraction, and cDNA collection.*S. cerevisiae* SC62 (YL-T3-rDNA::eGFP-TRP1-CYP5150L8-iGLCPR),[18] SC27 (SC62-eGFP::CYP512-W2^{I108A}-RFP),[19] YL-T3 (BY4742, Δ*trp1*, δDNA::tHMG1-LYS2, TRP::HIS-ERG20-ERG9-ERG1)[24] and its derivatives (Table S1) were grown at 30 °C and 220 rpm in either SC-His-Trp, SC-His-Leu, SC-His-Ura-Trp, SC-His-Leu-Ura, or SC-His-Leu-Ura-Trp as appropriate, or in YPD24 medium (containing 10 g/L of yeast extract, 20 g/L of beef peptone, 20 g/L of glucose, and 40 g/L glycerol) with appropriate concentrations of G418 and/or hygromycin for fermentation. *G. lucidum* was maintained on a potato dextrose agar slant. Precultivation and shake-static fermentation were performed at 30 °C.[26,27]

2.3. Extraction and Analysis of *Ganoderma* Metabolites. Dried mycelia were homogenized into powder using stainless steel beads in a tissue grinder (Jingxin, Shanghai, China) at 50 Hz for 5 min. About 10 mg of powder was extracted with 1 mL of ethyl acetate in an ultrasonic water bath for 30 min three times. After centrifugation at 12,000 *g* for 10 min, the supernatants were collected, dried under vacuum at 45 °C, and resuspended in 200 μL of methanol. After filtration through a 0.22 μm membrane, the subsequent filtrate was used for LC-MS analysis.

LC-MS analysis was conducted on an ACQUITY I-Class UPLC system (Waters, Wilmslow, UK) coupled to a SYNAPT XS ion mobility time-of-flight mass spectrometer (Waters, Wilmslow, UK). Mass Spectrometry parameters: ion source, ESI^- (negative mode); scan range, m/z 50−1200; source temperature, 150 °C; collision energy, 20−50 eV; cone voltage, 35 V; capillary voltage, 3.0 kV. The desolvation gas was nitrogen, with a temperature of 500 °C, a flow rate of 1000 L/h, and a gas pressure of 6.0 bar. Chromatographic separation was carried out on a Waters ACQUITY UPLC HSS T3 Column (2.1 × 100 mm, 1.8 μm). Mobile phase A was water with 0.1% formic acid, and mobile phase B was acetonitrile. A gradient elution program was applied as follows: 0 min, 20% B; 0−2 min, 20−26.5% B; 2−9 min, 26.5% B; 9−19 min, 26.5−35% B; 19−28 min, 35−60% B; 28−32 min, 60−70% B; 32−37 min, 70−90% B; 37−40 min, 90−100% B; 40−45 min, 100% B. The flow rate was 0.45 mL/min. The column temperature was 25 °C. One μL of sample was injected for analysis.

2.4. Coexpression Analysis. Coexpression analysis was performed using RNA sequencing data of*G. lucidum*mycelia in shake-static fermentation for 2, 8, and 12 days.[19] Linear regression analysis to calculate Pearson's correlation coefficient (PCC) on normalized expression levels was performed using R (version 4.0.2). Characterized genes responsible for GAs biosynthesis (*cyp5150l8*, *cyp512w2*, and *glat*) were used as bait genes.[19] The obtained list of strongly coexpressed genes (PCC > 0.6) was ranked in descending order of the mean PCC value of the three baits. FPKM values of genes were log_2-normalized for heatmapping using the NovoMagic platform (https://magic.novogene.com).

2.5. Candidate Gene Cloning. The total RNA from mycelia was extracted using Trizol and was reverse-transcribed to cDNA by FastKing RT Kit (TIANGEN, Beijing, China) according to the manufacturer's instructions. The full length of candidate genes was amplified by PCR using Phanta Max Super-Fidelity DNA Polymerase (Novoprotein, Nanjing, China) with*G. lucidum*cDNA as template. The PCR products were purified and inserted into expression vectors pRS426-HXT7p-FBA1t-G418r at the *PmeI*-site using Trelief SoSoo Cloning Kit (Tsingke, Beijing, China). Colony PCR was performed using 2 × Rapid Taq Master Mix (Novoprotein), and positive clones were validated by sequencing (GENEWIZ, Suzhou, China). All primers are listed in Table S3.

2.6. Yeast Transformation and Fermentation. The plasmids were transformed into yeast using the standard PEG/LiAc method.[28] Transformants were selected on an appropriate solid medium (SC medium without different amino acids). After incubation at 30 °C for 2−3 days, three colonies (unless otherwise indicated) were randomly picked and inoculated into 12 mL round-bottom test tubes containing 3 mL of the appropriate medium to an OD_{600} of 2.5−4. Then, they were inoculated into 12 mL round-bottom test tubes containing 3 mL of YPD24 or 250 mL shake-flasks containing 50 mL of YPD24 with appropriate concentrations of hygromycin and/or G418 at an initial OD_{600} of 0.05. Cell growth was determined by measuring the OD_{600} using a BioPhotometer (Eppendorf, Hamburg, Germany).

https://doi.org/10.1021/acscatal.5c04095
ACS Catal. 2025, 15, 13428−13443

After 120 h of fermentation, 1 mL of fermentation broth was mixed with 0.8 mL of ethyl acetate and vortexed for 3 min twice. After centrifugation at 12,000*g* for 10 min, the ethyl acetate supernatant was collected, concentrated in vacuo, and redissolved in methanol for HPLC analysis.

2.7. Yeast Microsome Isolation and In Vitro Enzymatic Assays. Yeast strain CYP512A13-r-iGLCPR-r and control strain CK-r-iGLCPR-r were used for microsome preparation. The strains were cultured in SC-His-Leu-Ura liquid medium for 24 h and transferred to 200 mL YPD24 medium containing 300 mg/L of G418 at an initial OD_{600} of 0.05. After 60 h of fermentation, yeast cells were harvested for microsome isolation.[24] The in vitro enzymatic reactions were carried out in a 500 μL system containing 90 mM Tris−HCl (pH 7.4), 2 mg of microsomal proteins, 2 mM NADPH, and different substrates (added in excess, with the exception of compound **3**, which was used in trace amounts). After incubation at 30 °C, 140 rpm for an appropriate duration, the products were extracted with an equal volume of ethyl acetate and analyzed by HPLC or UPLC-MS.

2.8. Analyses of Yeast Fermentation Extracts and In Vitro Enzymatic Reaction Products. HPLC analysis was conducted on an Agilent (Waldbronn, Germany) 1200 HPLC system equipped with an Agilent XDB-C18 column (4.6 μm, 5 × 250 mm). Mobile phase A was ultrapure water, and mobile phase B was methanol/acetic acid (100:0.1 v/v). A linear gradient of 80 to 100% B in 30 min at 1 mL/min was adopted. LC-MS was conducted on a UPLC (Waters, Wilmslow, UK), connected to a Q-TOF MS Premier in atmospheric pressure chemical ionization (APCI) positive ion mode, equipped with a Waters BEH C18 column (1.7 μm, 2.1 × 100 mm). Mobile phase A was ultrapure water/formic acid (100:0.1 v/v), and mobile phase B was methanol/formic acid (100:0.1 v/v). A linear gradient of 70 to 100% B in 10.5 min at 0.4 mL/min was adopted.

2.9. Liter-Scale Fermentation, Extraction, and Purification of Compounds. To obtain **1** and **2**, the yeast strain SC62-CYP512A13-r-CYP512W2-r was subjected to liter-scale fermentation. To obtain **3**, yeast strain SC27-L108D was subjected to liter-scale fermentation. After 5 days of fermentation, a total of 5 L of culture broth was harvested and mixed with 4 L of ethyl acetate. The cultures were mixed with a magnetic stirrer for 1 h to extract metabolites, and all extraction processes were repeated twice. After centrifugation, the ethyl acetate layer was collected, evaporated in vacuo, and redissolved in 20 mL of methanol for purification.

Purification of the crude extracts was first carried out on a preparative Agilent 1200 LC system. Mobile phase A was ultrapure water, and mobile phase B was methanol. In the first round of purification, a Kromasil 100−10-C18 column (20 mm × 250 mm) was used to purify **1** and **2**, while an Elite 100-C18 column (20 mm × 250 mm) was used to purify **3**. A linear gradient of 80 to 100% B in 30 min at 10 mL/min was adopted. In the second round of purification, **1** and **2** were purified using an Elite Hypersil ODS2 column (10 mm × 250 mm) with a linear gradient of 60 to100% B in 120 min at 4 mL/min. **3** was purified using a Kromasil 100-5-C18 column (21.2 × 250 mm) with a linear gradient of 50 to 100% B in 150 min at 4 mL/min. The third round of purification was first carried out on a Waters LC Prep 150 System (Milford, USA) with a Waters XBridge BEH C18 OBD Prep column (10 mm × 150 mm). A linear gradient of 50% to 100% B in 60 min at 6 mL/min was adopted for **1** and **3**, while a linear gradient of 60 to 100% B in 30 min at 6 mL/min was adopted for **2**. The elute with pure target compound was combined and concentrated with a rotary evaporator to a dry powder.

2.10. Nuclear Magnetic Resonance Analysis. One-dimensional and two-dimensional NMR spectra (^{1}H, ^{13}C, DEPT135, COSY, HSQC, HMBC, and NOESY) were measured on an Avance III 600 MHz Nuclear Magnetic Resonance instrument (Bruker, Karlsruhe, Germany). Compound **1** was dissolved in deuterated methanol (MeOD), and compound **2** was dissolved in deuterated chloroform ($CDCl_3$) for data acquisition. Chemical shifts (δ) were expressed in ppm, and coupling constants (J) were expressed in hertz (Hz). The NMR data were analyzed using MestReNova (version 14.0.0).

2.11. Model Construction. The structure of CYP512A13 complexed with heme was predicted by using the AlphaFold3 web server, and the protonation state of CYP512A13 was determined via PDB2PQR. Molecular docking of GA-Jb and THOLDOA into the active site of CYP512A13 was performed using AutoDock. Computational models for N107A and L108G were generated with PyMOL. For Compound I (Cpd I, Fe(IV)-oxo radical cation) and its axial cysteine, amber-compatible parameters developed by Cheatham et al. were assigned.[29] Parameters for GA-Jb and THOLDOA were generated using the Antechamber module with the General AMBER Force Field (GAFF). Partial charges were fitted to the electrostatic potential computed at the B3LYP/6-31G* level using the RESP model.

2.12. MD Simulations. Molecular dynamics (MD) simulations (three 100 ns replicas per model) were performed using pmemd.cuda in Amber 18.[30] First, all complex structures underwent a two-stage minimization process. In the initial 5000 cycles, the conjugate gradient method was employed, allowing only solvent and hydrogen atoms to move. Subsequently, an additional 5000 cycles of minimization were carried out without restraints. The systems were then gradually heated from 0 to 300 K throughout 100 ps, followed by 200 ps of equilibration under constant pressure and temperature conditions. Finally, three independent 100 ns classical MD simulations were conducted for each system. The SHAKE algorithm was applied to constrain the motion of water molecules and maintain fixed hydrogen bond angles. Long-range electrostatic interactions were treated using the particle-mesh Ewald method with a cutoff of 10 Å for both Lennard-Jones and electrostatic interactions.

2.13. QM Calculations. All calculations were performed using Gaussian 16.[31] Quantum mechanics (QM) models were constructed by extracting the substrate, truncated heme, and cysteine from the GA-Jb-CYP512A13 complex. Geometry optimizations and frequency calculations were carried out at the B3LYP level. The LANL2DZ basis set was used for iron, while the 6-31G* basis set was used for all other atoms. Free-energy correction values (Gcorr) were obtained from frequency calculations. The B3LYP/6-311G** density functional theory (DFT) method was used for single-point energy calculations (E). The sum of E and Gcorr was defined as the free energy G and utilized for comparing the relative stabilities of different species.

2.14. QM/MM Calculations. The H-abstraction mechanism of CYP2A13-catalyzed GA-Jb to enones was further investigated using a two-layer quantum mechanics/molecular mechanics (QM/MM) approach. The initial enzyme−substrate complex geometry was extracted from clustered

https://doi.org/10.1021/acscatal.5c04095
ACS Catal. 2025, 15, 13428−13443

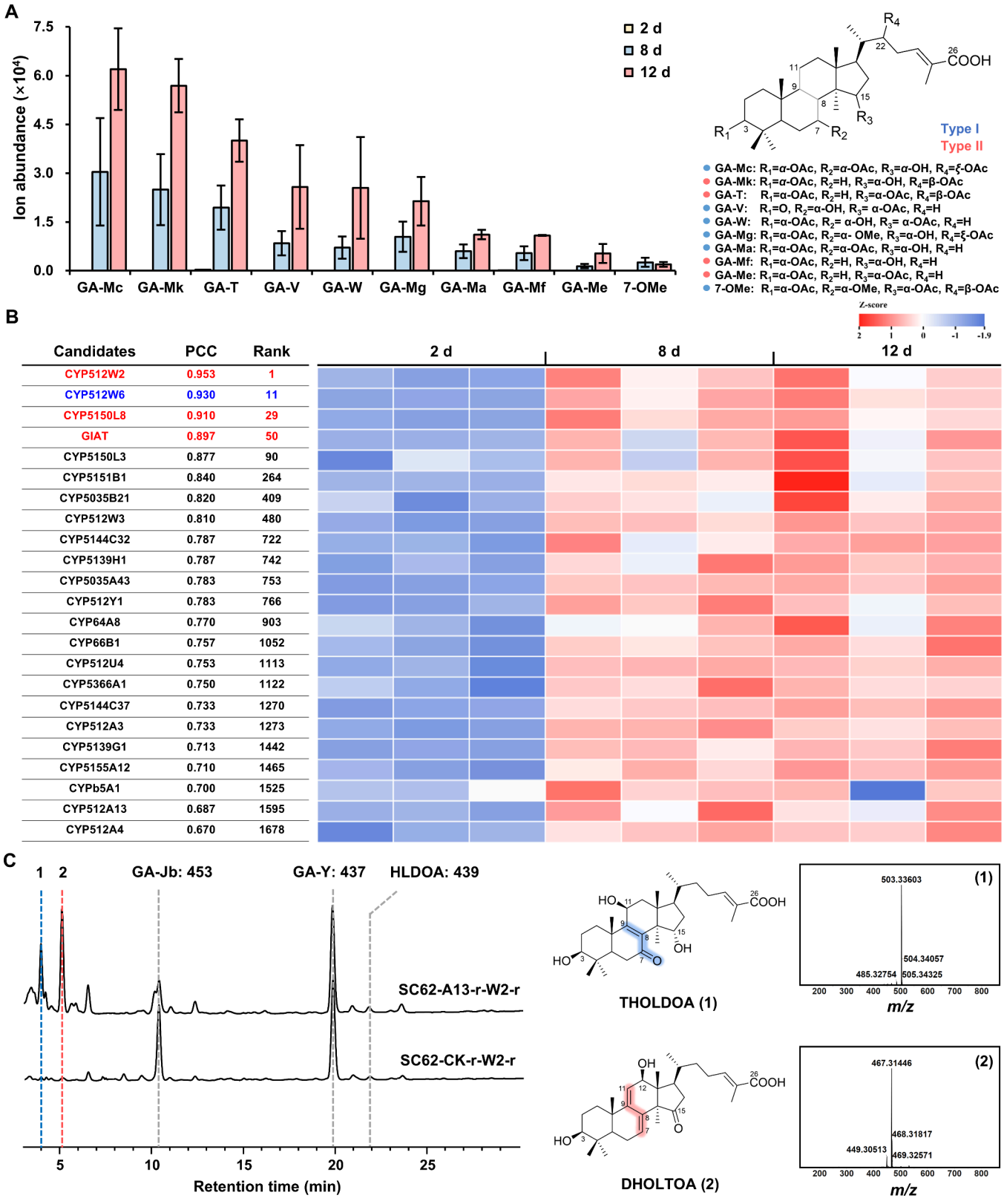

Candidates	PCC	Rank
CYP512W2	0.953	1
CYP512W6	0.930	11
CYP5150L8	0.910	29
GIAT	0.897	50
CYP5150L3	0.877	90
CYP5151B1	0.840	264
CYP5035B21	0.820	409
CYP512W3	0.810	480
CYP5144C32	0.787	722
CYP5139H1	0.787	742
CYP5035A43	0.783	753
CYP512Y1	0.783	766
CYP64A8	0.770	903
CYP66B1	0.757	1052
CYP512U4	0.753	1113
CYP5366A1	0.750	1122
CYP5144C37	0.733	1270
CYP512A3	0.733	1273
CYP5139G1	0.713	1442
CYP5155A12	0.710	1465
CYPb5A1	0.700	1525
CYP512A13	0.687	1595
CYP512A4	0.670	1678

Figure 2. CYP512A13 was found to biosynthesize different types of GAs. (A) Ion abundance of different types of GAs detected from*G. lucidum*fermentation samples. All data represent the mean of three biologically independent samples, and the error bars show the standard deviation. (B) Transcriptomic analysis of*G. lucidum*for identifying enzyme candidates. Coexpression analysis of*G. lucidum*RNA samples after 2, 8, and 12 d in shake-static fermentation by using *cyp5150l8*, *cyp512w2*, and *glat* as bait genes. Linear regression analysis is used to screen genes with Pearson's correlation coefficient (PCC) > 0.6 with baits. PCC values are averages calculated using three baits. Enzymes highlighted in red refer to the baits used for the analysis, and enzymes highlighted in blue indicate the characterized enzymes in GA's biosynthesis. For the remaining candidates, see Table S2. (C) LC-MS analysis of 120 h fermentation extracts of strains SC62-W2-r-A13-r and SC62-W2-r-CK-r. The enone structure and conjugated double bonds are highlighted in blue and red, respectively.

https://doi.org/10.1021/acscatal.5c04095
ACS Catal. 2025, 15, 13428−13443

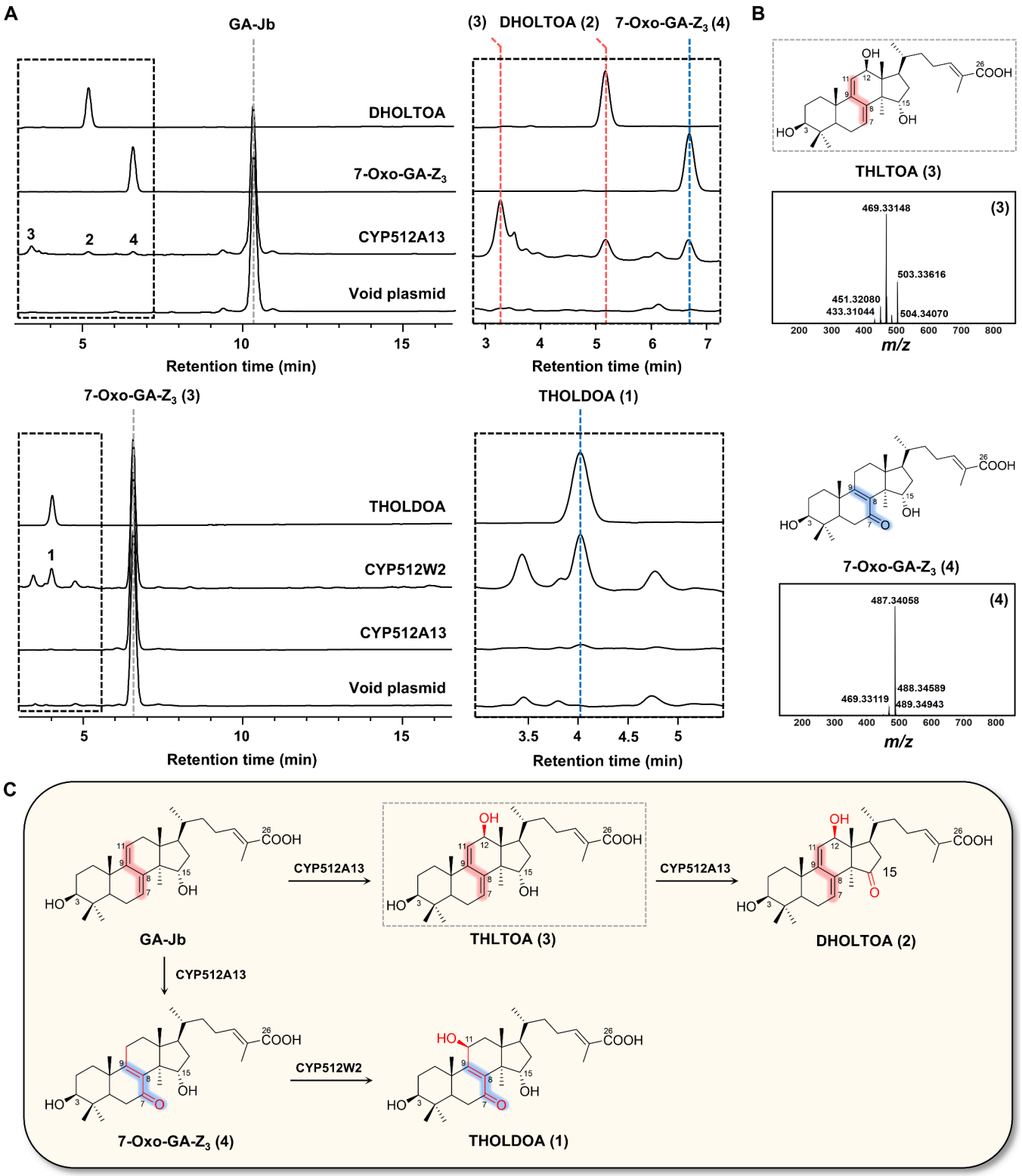

Figure 3. CYP512A13 interconverts different types of GAs. (A) HPLC analysis of the *in vitro* enzymatic extracts by incubating the CYP512A13 and CYP512W2 containing microsomes with different substrates (left), with the enlarged view highlighted in the black dotted line frame in the left (right). Void plasmid indicates the microsomes prepared from the control strain CK-r-iGLCPR-r. (B) Mass information on **3** and **4**. (C) Proposed conversion of GA-Jb into **1** to **2** by CYP512A13 and CYP512W2. The predicted structure of **3** is indicated in the gray dashed box. The enone structure and the conjugated double bonds are highlighted in blue and red, respectively.

MD trajectories, with the system truncated to include only protein residues and water molecules within 5 Å of the GA-Jb substrate, containing a total of 921 atoms. Notably, 160 atoms comprising the reactive center (including GA-Jb, heme, parts of cysteine, and a water molecule) were treated at the QM level using the DFT method, representing one of the most extensive QM regions employed in P450 QM/MM studies to date. All calculations were performed using Gaussian 16

https://doi.org/10.1021/acscatal.5c04095
ACS Catal. 2025, 15, 13428−13443

software. The MM region was described using the AMBER force field with TIP3P water parameters, while GA-Jb and the heme group retained their original MD simulation parameters. Geometry optimizations and frequency calculations were conducted using the mechanical embedding (ONIOM-ME) scheme at the B3LYP/6-31G* level, followed by higher-level single-point energy calculations employing electronic embedding (ONIOM-EE) with the B3LYP/6-311G** basis set.

3. RESULTS

3.1. Discovery of CYP512A13 with the Capability To Biosynthesize Different Types of GAs in Yeast. The static-shake culture of*G. lucidum*served as a canonical strategy to stimulate type II GAs biosynthesis during *Ganoderma* mycelium fermentation.[26,27] In this study, to investigate whether this cultural strategy could also enhance the production of type I GAs, we re-examined our previously cryopreserved fermentation samples. As shown in Figure 2A, we detected distinctive ionic fragment signal characteristics corresponding to six type I GAs (GA-Mc, GA-V, GA-W, GA-Mg, GA-Ma, and 7-*O*-methyl ganoderic acid O (7-OMe)) after 2, 8, and 12 days of fermentation through the mass spectrometer. Although none of them has formed a C7 carbonyl group, C7 oxidative modification occurred, representing a possible postmodification before enone formation. Of all the detected type I GAs, C26 carboxylation, C15 hydroxylation, and/or C15 O-acetylation occur concurrently (Figure 2A). These findings indicated that the key missing enzyme for the formation of the enone structure at C7, C8 and C8, C9 may exhibit a similar expression pattern with C26 oxidase CYP5150L8,[24] C15 hydroxylase CYP512W2,[18] and C15 *O*-acetylase GlAT[19] under the same fermentation conditions.

Next, we used *cyp5150l8*, *cyp512w2*, and *glat* as bait genes for coexpression analysis of*G. lucidum*mycelia transcriptome data after 2, 8, and 12 days of shake-static fermentation. A total of 1752 transcripts were highly coexpressed with three baits. Among them, 20 CYPs were identified (Figure 2B and Table S2). Excluding CYP512W6 with known function,[19] 19 CYPs form the data set of candidates. After several attempts under different PCR conditions, we failed to obtain the coding regions of 7 CYPs, which exhibited no amplification or early termination (Table S3).

To test whether the remaining 12 CYPs could catalyze the formation of the enone of type I GA, we individually introduced the CYP-expressing plasmids into*Saccharomyces cerevisiae*strain SC62-CYP512W2-r (the HLDOA-producing strain SC62 carries a plasmid expressing CYP512W2), which was able to generate multiple possible substrates, ganoderic acid HLDOA and GA-Jb, simultaneously.[18] Compared with the control strain SC62-CK-r-CYP512W2-r (the HLDOA-producing strain SC62 harbors two plasmids: one expressing CYP512W2 and the other a void plasmid), only the CYP512A13-expressing strain SC62-CYP512A13-r-CYP512W2-r (the HLDOA-producing strain SC62 harbors two plasmids: one expressing CYP512W2 and the other expressing CYP512A13) generated two products, with primary m/z values at 503 (peak **1**) and 467 (peak **2**), respectively, concomitant with the significant reduced accumulation of GA-Jb in LC-MS analysis of 120 h fermentation extracts (Figure 2C). For product **1**, with an increased m/z of 64 compared to that of HLDOA, we speculated that it may correspond to the product after multiple oxidations of HLDOA. For product **2**, with an increased m/z of 14 compared to that of GA-Jb, we speculated that it may correspond to the product after hydroxylation and dehydrogenation of GA-Jb. We further performed 5 L fermentation of strain SC62-CYP512A13-r-CYP512W2-r, obtained 1.9 mg of **1** and 1.8 mg of **2** from the fermentation extracts, and confirmed their structures by NMR analyses. Compound **1** was identified as 3β,11β,15α-trihydroxy-7-oxo-lanosta-8,24-dien-26-oic acid (THOLDOA) (Table S4 and Figures S3−S9). Compound **2** was identified as 3β,12β-dihydroxy-15-oxo-lanosta-7,9(11),24-trien-26-oic acid (DHOLTOA) (Table S4 and Figures S10−S16). A pair of carbon−oxygen conjugated double bonds was generated at C8, C9 and C7, C8 on the cyclic skeleton of THOLDOA, forming the enone structure of type I GA. For DHOLTOA, C12 hydroxylation and C15 oxidation occurred at the type II GA's skeleton. To the best of our knowledge, both of them were unreported GAs.

3.2. Investigation into the Biosynthetic Routes toward the Interconversion between Different Types of GAs. To understand the biosynthetic steps by which CYP512A13 is involved in the formation of different GA types, we prepared yeast microsomes containing either the CYP512A13 expression plasmid or the void plasmid and conducted *in vitro* reactions using the purified compounds as substrates. When the mixture was reacted with HLDOA and GA-Y, no new peaks were detected in comparison to those from the yeast microsomes containing the void plasmid (Figure S17). These results suggested that both HLDOA and GA-Y might not be the preferred substrates of CYP512A13. In contrast, three new peaks were detected when GA-Jb was tested (Figure 3A). The retention time and mass spectrometry information on peak **2** were completely consistent with those of **2** identified in the fermentation assay (Figures 3A and 2C). Compared with the primary m/z 453 of GA-Jb, an increased m/z value of 16 as detected in peak **3** suggested that a hydroxyl group was added in **3**. Compared with the primary m/z 467 of **2**, two additional hydrogen atoms were incorporated in peak **3**, which indicated that different oxidation forms on C15 existed between **2** and **3**. We speculated that peak **3** may correspond to reaction intermediate 3β,12β,15α-trihydroxy-lanosta-7,9(11),24-trien-26-oic acid (THLTOA) (Figure 3A,B). As for peak **4**, it exhibited the same retention time and mass spectrometry characteristics as our previously identified GA 7-oxo-GA-Z_3.[18] Compared with the chemical structure of **1** identified from the fermentation extracts, the lack of C11 hydroxylation was observed on **4**. Thus, we speculated that **4** serves as the direct precursor of **1**. In our previous study, CYP512W2 was identified as an oxidase capable of oxidation at C7, C11, and C15.[18] Here, to explore whether CYP512A13 or CYP512W2 could catalyze the conversion of **4** into **1**, we also prepared CYP512W2-containing yeast microsomes. When **4** was incubated with different CYPs, only CYP512W2 could generate **1** in the reaction extracts (Figure 3A,B).

To determine the order of oxidation, we first investigated the time-dependent reaction profile of CYP512A13 with GA-Jb. Within the first 2 h, peaks **3**, **2**, and **4** appeared rapidly, accompanied by a substantial depletion of GA-Jb (Figure S18A). By 18 h, peak **4** exhibited further accumulation, whereas the levels of peaks **3** and **2** remained nearly constant (Figure S18A). To clarify the catalytic relationship between **3** and **2**, we successfully isolated and purified a trace amount of **3** for use as a substrate in subsequent *in vitro* reactions. After 18 h incubation with CYP512A13, **3** was nearly completely

https://doi.org/10.1021/acscatal.5c04095
ACS Catal. 2025, 15, 13428−13443

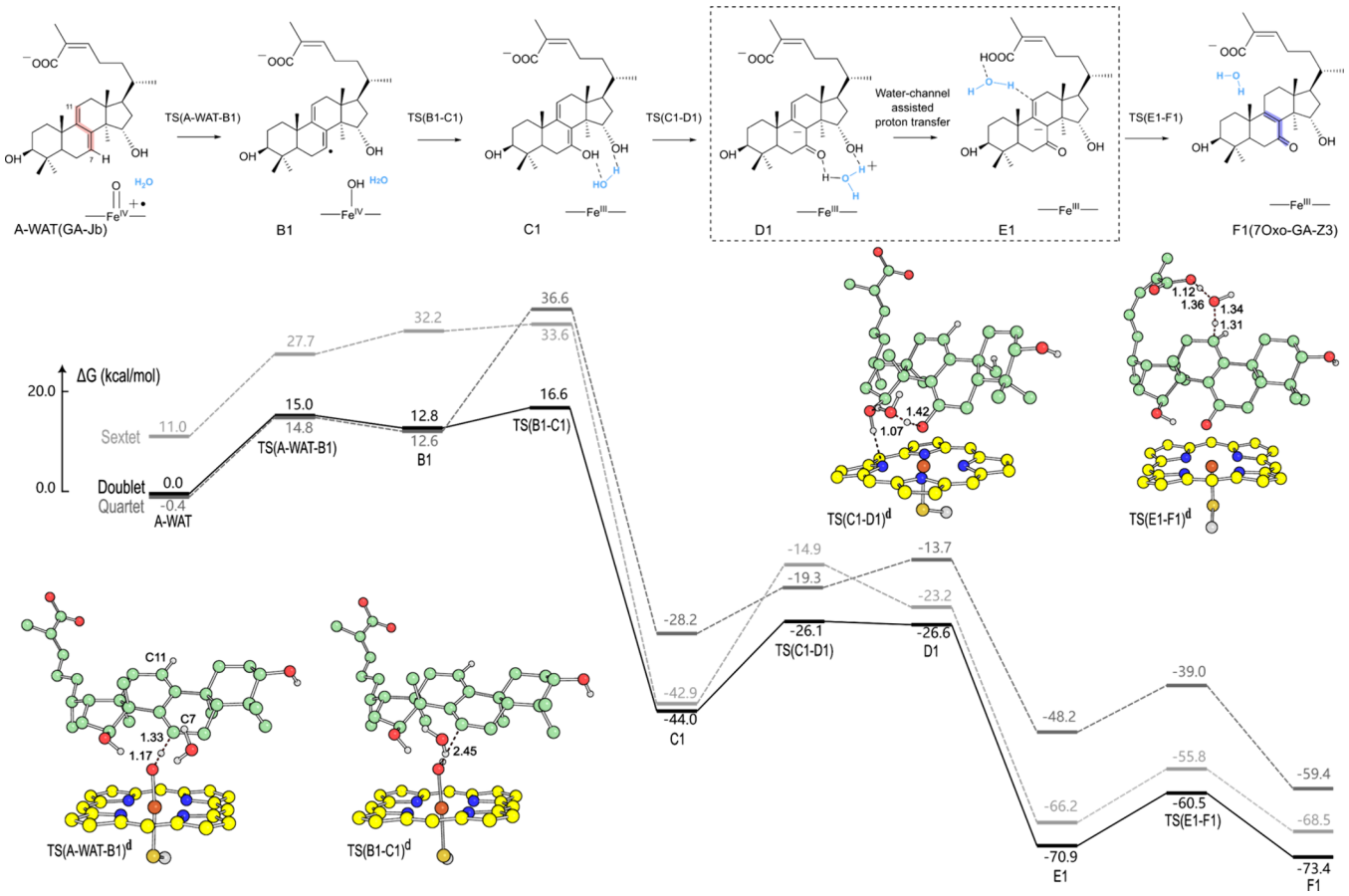

Figure 4. Water-assisted H-abstraction mechanism and energy landscape for the conversion of GA-Jb to 7-oxo-GA-Z_3 at doublet, quartet, and sextet states. Key transition states (TS(A-WAT-B1)^d, TS(B1−C1)^d, TS(C1-D1)^d, and TS(E1-F1)^d) are shown (substrate carbons (pale green spheres) and heme (yellow spheres)).

converted to **2**, whereas CYP512W2 showed no catalytic activity under the same conditions (Figure S18B). Notably, when **2** was used as the substrate, neither CYP512A13 nor CYP512W2 mediated further transformation (Figure S18C), effectively ruling out the possibility of **3** being converted from **2**.

Based on the results of *in vivo* fermentation and *in vitro* biochemical characterization, we propose the biosynthetic routes to different GAs by CYP512A13. On one hand, CYP512A13 hydroxylates GA-Jb at C12 to form the intermediate **3** and then further rapidly oxidizes the C15 hydroxyl group of **3** to form a keto group, resulting in a type II GA with a more complicated structure (Figure 3C). On the other hand, CYP512A13 can catalyze the oxidation at C7 of GA-Jb, which triggers the migration of conjugated double bonds at C7, C8 and C9, C11, to generate the enone structure of **4**. Then, CYP512W2 can hydroxylate C11 of **4** to form the novel type I GA THOLDOA (Figure 3C).

3.3. Computational Exploration of the Catalytic Mechanism of CYP512A13 and Determination of the Dominant Reaction Pathway. To elucidate the catalytic mechanism of CYP512A13, we employed AlphaFold3 to predict the CYP512A13-heme structure. A comparative structural analysis with CYP512W2, a monooxygenase that converted HLDOA to GA-Y and GA-Jb as reported in our previous work,[32] revealed that although both enzymes have nearly identical folding patterns, CYP512A13 features a larger and more hydrophilic intersection extended from the active pocket and the substrate access channel (Figure S19). Molecular docking of GA-Jb into CYP512A13 identified two primary binding conformations, named C7 and C12 poses, where the positions of C7 and C12 were close to the active oxygen of Cpd I, respectively. Oxidation at C7 generates 7-oxo-GA-Z_3, while C12 oxidation forms type II GAs (**3** and DHOLTOA). We further docked **3** into CYP512A13 with the C15 pose for ketonization, ultimately forming DHOLTOA (Figure S20).

The conversion of GA-Jb to 7-oxo-GA-Z_3 involved C7 oxidation, which induced conjugated double bond migration. Through QM calculations for the doublet, quartet, and sextet states, it was found that structure A exhibits the lowest energy in the quartet state, but it was only 0.2 kcal/mol lower than that of the doublet state in the Gibbs free energy. Considering the doublet state remained energetically favorable throughout most reaction steps, we utilized it as the reference for constructing the energy landscape toward enone (7-oxo-GA-Z_3) formation. The reaction is initiated with active oxygen of Cpd I attacking the C7 position of the conjugated double bond, forming a C7−O bond (TS(A-B)^q, $\Delta^{\ddagger}$ = 11.5 kcal/mol; "d/q/s" denote doublet/quartet/sextet states). After the first transition state, spin crossover occurred, and three sequential hydrogen transfers occurred along the tetracyclic skeleton: C7 to C8 (TS(B−C)^d), C8 to C9 (TS(C−D)^d), and C9 to C11 (TS(D-E)^d). The notably high barrier for C8 to C9 hydrogen transfer (TS(G-H)^d, $\Delta^{\ddagger}$ = 48.6 kcal/mol) made this pathway

https://doi.org/10.1021/acscatal.5c04095
ACS Catal. 2025, 15, 13428−13443

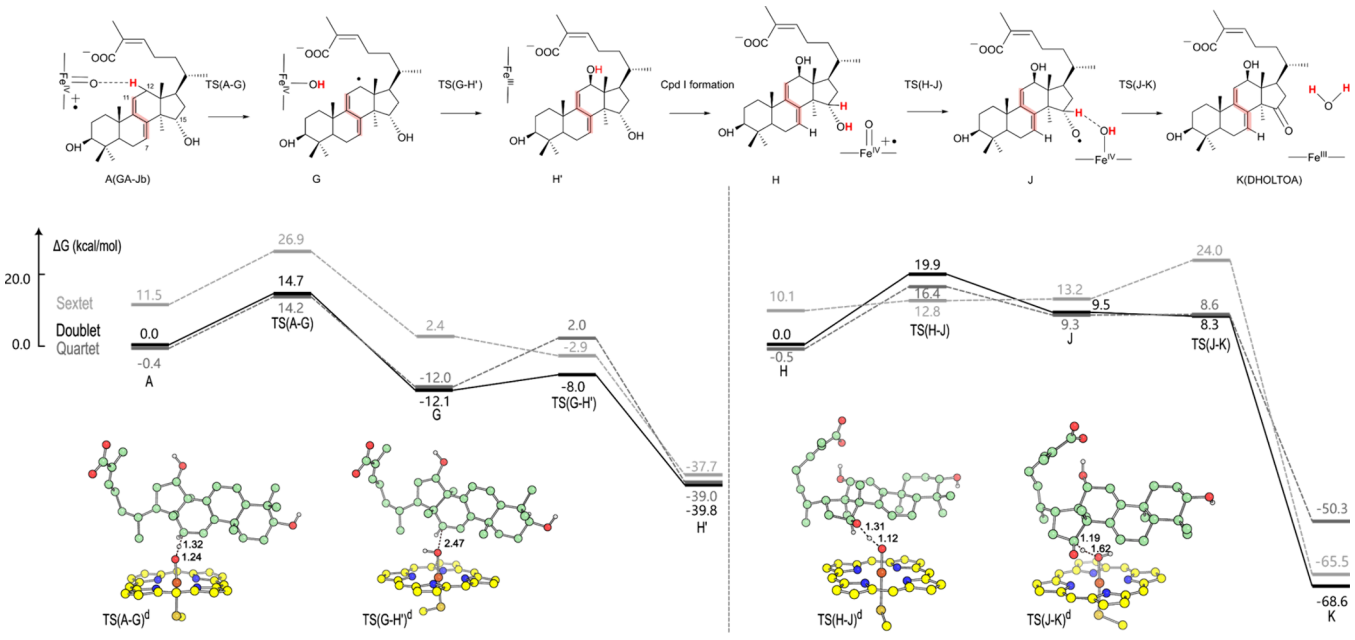

Figure 5. Reaction mechanism and energy landscape for the conversion of GA-Jb to DHOLTOA at doublet, quartet, and sextet states. The left panel shows the C12 hydroxylation process. The right panel shows the C15 ketonization process for Route 1. Key transition states (TS(A-G)^{d}, TS(G-H')^{d}, TS(H-J)^{d}, TS(J-K)^{d}) are shown (substrate carbons (pale green spheres) and heme (yellow spheres)).

energetically unfavorable (Figures S21−S24 and Tables S5−S7, S15−S17, S25−S27).

Considering the hydrophilic characteristics of CYP512A13's active pocket, we explored two water-assisted pathways: H-abstraction and O-attack (Figures 4 and S25−S28). For both pathways, the doublet was identified as the dominant ground state and was utilized as a reference for the whole reaction. Although the quartet of the first three structures (A-WAT, TS(A-WAT-B1), TS(A-WAT-B2), and B1) displayed slightly lower (0.2−0.6 kcal/mol) energy than the doublet, the subtle energy difference was not considered in detail here (Figure 4).

The H-abstraction pathway was initiated with H-abstraction from C7 (TS(A-WAT-B1)^{d}, $\Delta G^{\ddagger}$ = 15.0 kcal/mol), followed by hydroxyl rebound to form intermediate C1 ($\Delta G^{\ddagger}$ = 16.6 kcal/mol). A water-mediated hydrogen bond network (involving C7/C15 hydroxyls, water, and the nitrogen atom of heme) significantly stabilized the transition state for enone formation (TS(C1-D1)^{d}, $\Delta G^{\ddagger}$ = 17.9 kcal/mol). The pathway ended with carboxyl-assisted proton transfer to C11 (TS(E1-F1)^{d}, $\Delta G^{\ddagger}$ = 10.4 kcal/mol). In contrast, the O-attack pathway began with direct C7−O bond formation, and then hydrogen transfer from C7 to C8 proceeded. The water-mediated hydrogen bond network (involving C15 hydroxyl, water, and the nitrogen atom of heme) facilitated the C8 hydrogen removal reaction with an energy barrier of 22.3 kcal/mol. Similarly, the pathway terminated with proton transfer to C11, as the H-abstraction pathway. Computational results showed that the H-abstraction pathway was more favorable than the O-attack pathway (Figure S25 and Tables S8−S10, S18−S20, S28−S30), with its rate-determining step exhibiting a lower energy barrier (17.9 kcal/mol vs 22.3 kcal/mol).

The conversion of GA-Jb to DHOLTOA proceeded through C12 hydroxylation (TS(A-G)^{q}) and the hydroxyl rebounded (TS(G-H')^{d}), yielding **3**. After that, the Cpd I was regenerated and continued to oxidize the C15 hydroxyl of **3** to DHOLTOA via two possible pathways (Figures 5 and S29−S32). Route 1 involved consecutive hydrogen abstraction reactions, starting with the removal of the hydrogen from the C15 hydroxyl, followed by the removal of the hydrogen from C15 itself. Finally, radical recombination occurred, leading to the formation of the product DHOLTOA (Figure 5). The rate-determining step of this reaction was the first step, and the energy of TS(H-J) was 12.8 kcal/mol. In Route 2, reactions proceeded via H-abstraction and hydroxyl rebound as well as dehydration of the geminal-diol intermediate. The energy barrier of Route 2 was 16.1 kcal/mol (Figure S29, TS(H−I)^{d}, Tables S11−S13, S21−S23, S31−S33).

In all, the energy barrier for the formation of 7-oxo-GA-Z_3 was calculated to be 17.9 kcal/mol in the H-abstraction pathway and 22.3 kcal/mol in the O-attack pathway by QM calculations, demonstrating the energetic preference for the former. For the generation of DHOLTOA, C12 hydroxylation was decisive (14.6 kcal/mol), and the subsequent ketonization of C15 proceeded via consecutive hydrogen abstraction reactions.

To better characterize the molecular dynamics of GA-Jb within the enzyme active pocket, we constructed three models: GA-Jb in the C7 pose complexed with CYP512A13 (GA-Jb-C7/CYP512A13 for enone formation), GA-Jb in the C12 pose complexed with CYP512A13 (GA-Jb-C12/CYP512A13 for THLTOA formation), and THLTOA in the C15 pose complexed with CYP512A13 (GA-Jb-C15/CYP512A13 for DHOLTOA formation). Key features derived from the TS calculated by the DFT method were employed to evaluate the feasibility of the pathway.

For the GA-Jb-C7/CYP512A13 model, we defined prereactive states (PRSs) for the H-abstraction pathway (D(O−H_{C7}) < 3.0 Å, 100° ≤ A(Fe−O−H_{C7}) ≤ 140°, and 140° ≤ A(C7−H_{C7}-O) ≤ 180°, where D represented distance and A represented angle) and for the O-attack pathway (D(O−C7) < 3.0 Å, 70° ≤ A(O−C7−H_{C7}) ≤ 110°, and 70° ≤ A(O−C7−C8) ≤ 110°). MD simulations revealed that the PRSs percentage for the C7 H-abstraction conformation was 93.16%, whereas that for the C7−O attack was merely 0.01%.

https://doi.org/10.1021/acscatal.5c04095
ACS Catal. 2025, 15, 13428−13443

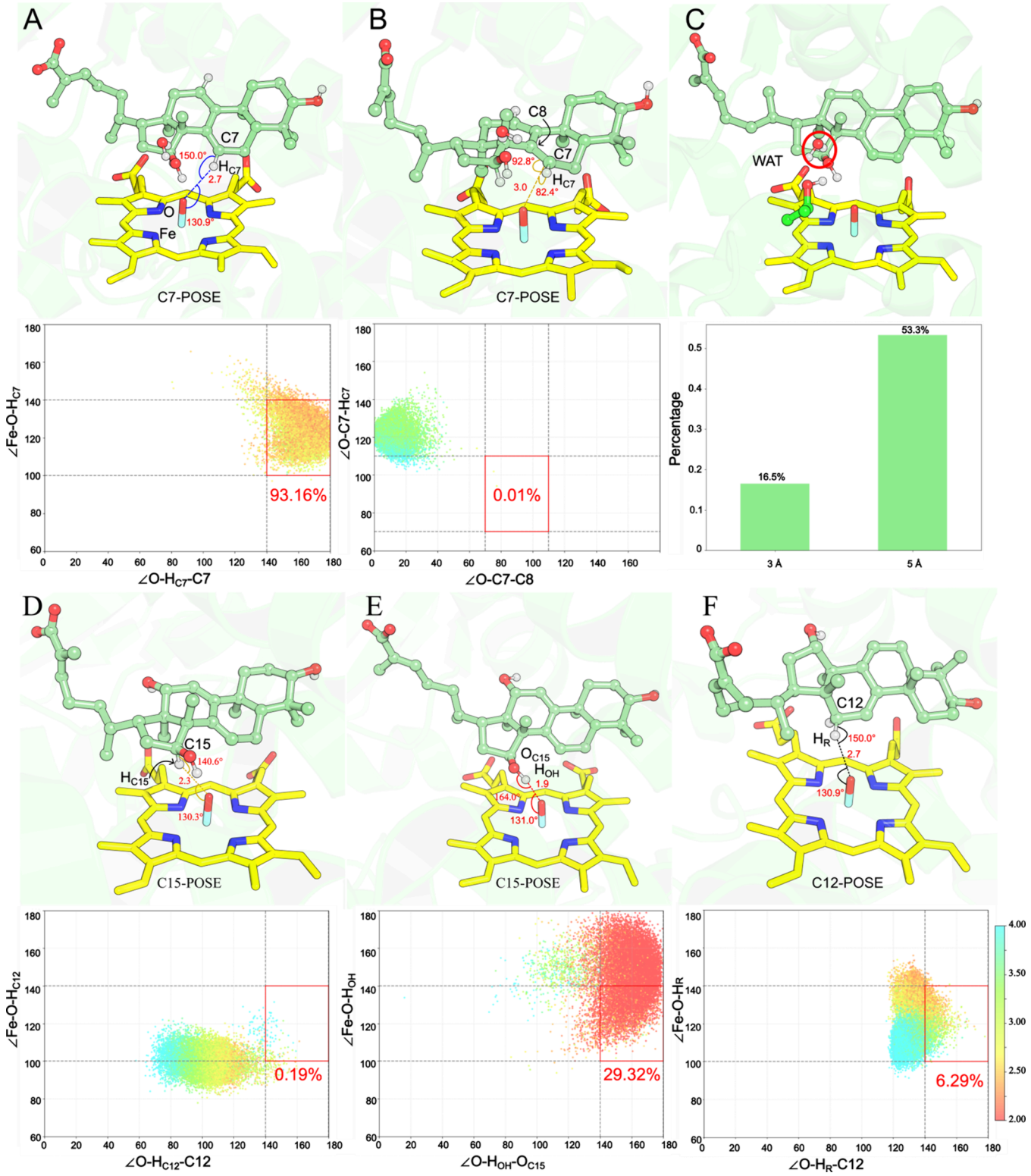

Figure 6. Mechanistic understanding of reactive pathways and hydration dynamics from MD simulations. (A) C7H-abstraction pathway in the GA-Jb-C7/CYP512A13 model: representative structures and PRS distribution. (B) C7−O attack pathway in the GA-Jb-C7/CYP512A13 model: representative structures along with PRS distribution. (C) Water probability around the C15-OH group (3 and 5 Å radii). (D) GA-Jb-C12/CYP512A13 model trajectories and PRS distribution. (E) THLTOA-C15/CYP512A13 model (Route 1) with PRS analysis. (F) THLTOA-C15/CYP512A13 model (Route 2) with PRS analysis.

This strongly suggested that the H-abstraction pathway was favorable for enone formation (Figure 6A,B). Additionally, as highlighted by the QM calculations, the hydrogen bond network between water molecules and C15 hydroxyl displayed a critical role of water in this process. MD trajectories indicated the proportions of water molecules within 3 and 5 Å of the C15 hydroxyl oxygen were 16.5 and 53.3%, respectively (Figure 6C and Movie S1). For the GA-Jb-C12/CYP512A13

https://doi.org/10.1021/acscatal.5c04095
ACS Catal. 2025, 15, 13428−13443

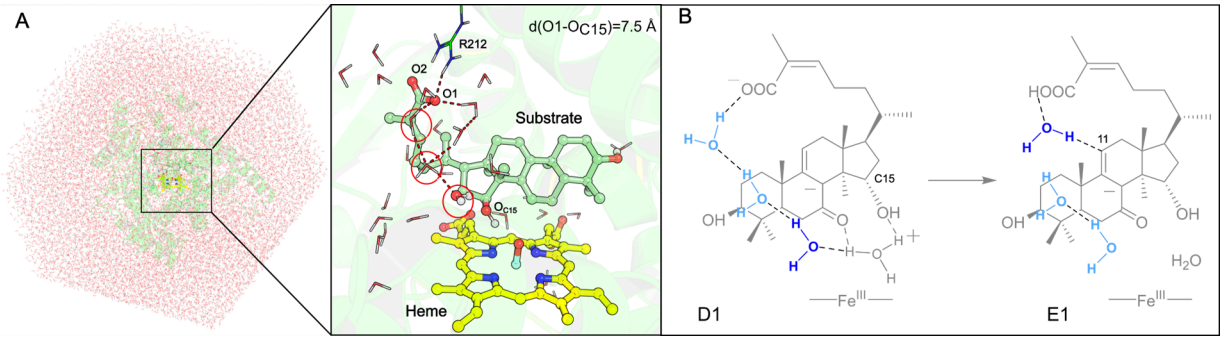

Figure 7. Representative structure from clustered MD simulations for QM/MM calculations and schematic for proton transfer from the hydroxyl of C15 to the carboxyl. (A) Most representative structure from three clustered MD simulations. The amplification of the active site. Residue R212 forms a hydrogen bond with the carboxyl of the substrate, and three water molecules form a water channel between the hydroxyl of C15 and the carboxyl. The high layer was shown as sticks and spheres (heme, substrate, one water, and $-SCH_3$ of C443). (B) Schematic of three water-mediated proton transfer reactions (real situation in MD simulations and QM/MM calculations).

model, the PRSs percentage ($D(O-H_R) < 3.0$ Å, $100° \leq A(Fe-O-H_R) \leq 140°$, and $140° \leq A(C12-H_R-O) \leq 180°$) was 6.3%, indicating the feasibility of C12 hydroxylation (Figure 6D). In the C15 ketonization process, the PRSs percentages ($D(O-H_{C15}) < 3.0$ Å, $100° \leq A(Fe-O-H_{C15}) \leq 140°$, $140° \leq A(C15-H_{C15}-O) \leq 180°$) were 29.3% for Route 1 and 0.19% for Route 2, highlighting the dominance of Route 1 (Figure 6E,F).

To assess the potential influence of the enzymatic microenvironment on the water-assisted mechanism of THOLDOA formation, QM/MM calculations were performed based on the most representative structure from clustered MD simulations of the GA-Jb-C7/CYP512A13 complex. This structure revealed a water channel of three molecules bridging the C15 hydroxyl and carboxyl of GA-Jb, facilitating the proton transfer from D1 to E1 (Figures 7 and S33).

As indicated by QM computational results that overall reactions proceed mainly in the doublet state, the QM/MM calculations were carried out in the doublet. Similar to QM calculations, the QM/MM confirmed the favorable H-abstraction pathway, with TS(C1−D1)[d] showing an energy barrier of 19.1 kcal/mol (Figure S34, S35 and Tables S14, S24, S34). Comparison of the structure of D1 with that of E1 revealed that the carboxyl group (including O1 and O2) underwent a 3.3 Å movement from D1 to E1, while maintaining the salt bridge with R212, although the interaction shifted from O2 in D1 to O1 in E1 (Figure S36A). The protonated O2 formed a new hydrogen bond with a water molecule, positioning its hydrogen 3.5 Å from C11, facilitating the subsequent proton transfer (Figure S36B). MD simulations demonstrated that R212 formed a weak salt bridge with the carboxyl group of GA-Jb. The salt bridge remained at low percentages (10.9% for O1_H12 and 33.06% for O2_H22, Figure S37A,C), suggesting their interactions were not solid enough. This was mainly due to the surrounding water molecules (Figure S37B), which enabled the slight movement of the carboxyl tail. These results demonstrated the water-assisted mechanistic plausibility within the enzyme pocket.

3.4. Identification of Key Residues for the Substrate Specificity of CYP512A13. We performed an energy decomposition analysis based on MD trajectories to pinpoint the key residues that govern substrate selectivity. This analysis led to the identification of five critical residues—L108, V110, V111, R212, and A297—that made substantial contributions to substrate binding, with each residue contributing a binding energy exceeding 1.0 kcal/mol (Figure 8A). Considering that the I108A mutation in CYP512W2 (structurally equivalent to N107 in CYP512A13) enhanced the enzymatic activity (28), we included N107 in our analysis. These six residues were proposed as pivotal regulators of catalytic efficiency and product distribution between enones and type II GAs (Figure 8B). For the L108 position, we evaluated five variants (L108A, L108G, L108D, L108E, L108N) with occurrence frequencies greater than 8%, based on a multiple sequence alignment of 150 homologous sequences. Both L108D and L108E could form hydrogen bonds with the C3 hydroxyl. However, L108D was prioritized due to its shorter side chain. This shorter side chain offered greater spatial flexibility, which could increase the $A(O-H_R-C12)$ angle to enhance the C12 hydroxylation (predominantly less than 140° in the WT). This change might potentially enhance the selectivity for type II GA (Figure S38). To streamline experimental validation, we selected L108A, L108G, L108D, and L108N for further analysis, excluding L108E. For V110, five high frequency variants (V110A, V110L, V110F, V110S, and V110T) were evaluated. V110F was excluded due to its bulky side chain, while V110T was chosen due to its relatively high frequency and structural similarity to V110S. V111L (with an occurrence frequency of 40.8%) and R212A (37.3%) were solely selected because their frequencies were significantly higher than those of other variants (Figure S39). For N107 and A297, which were located at the back and front of the tetracyclic ring skeleton, respectively, small side chain residues (N107A, N107G, N107S, and A297G and A297S) were chosen for mutation (Figure S40).

To assess the functional impact of these mutations, we expressed CYP512A13 and its variants in the GA-Jb-producing yeast strain SC27, a yeast strain capable of stably producing GA-Jb,[19] as the starting strain for the *in vivo* assay. The expression plasmids of CYP512A13 and its variants, along with the void plasmid, were individually introduced into SC27. This led to the generation of strains SC26-WT, SC27-N107A, SC27-N107G, SC27-N107S, SC27-L108A, SC27-L108D, SC27-L108G, SC27-L108N, SC27-V110A, SC27-V110L, SC27-V110T, SC27-V111L, SC27-R212A, SC27-A297G, SC27-A297S, and SC27-CK, respectively (Table S1). Compared to the control strain, the major fermentation products of CYP512A13 and most of its variants were THOLDOA, 7-oxo-GA-Z_3, and DHOLTOA (Figure S41). For WT and these variants, the production levels of THOLDOA and 7-oxo-GA-Z_3 reflected the C7 oxidation

https://doi.org/10.1021/acscatal.5c04095
ACS Catal. 2025, 15, 13428−13443

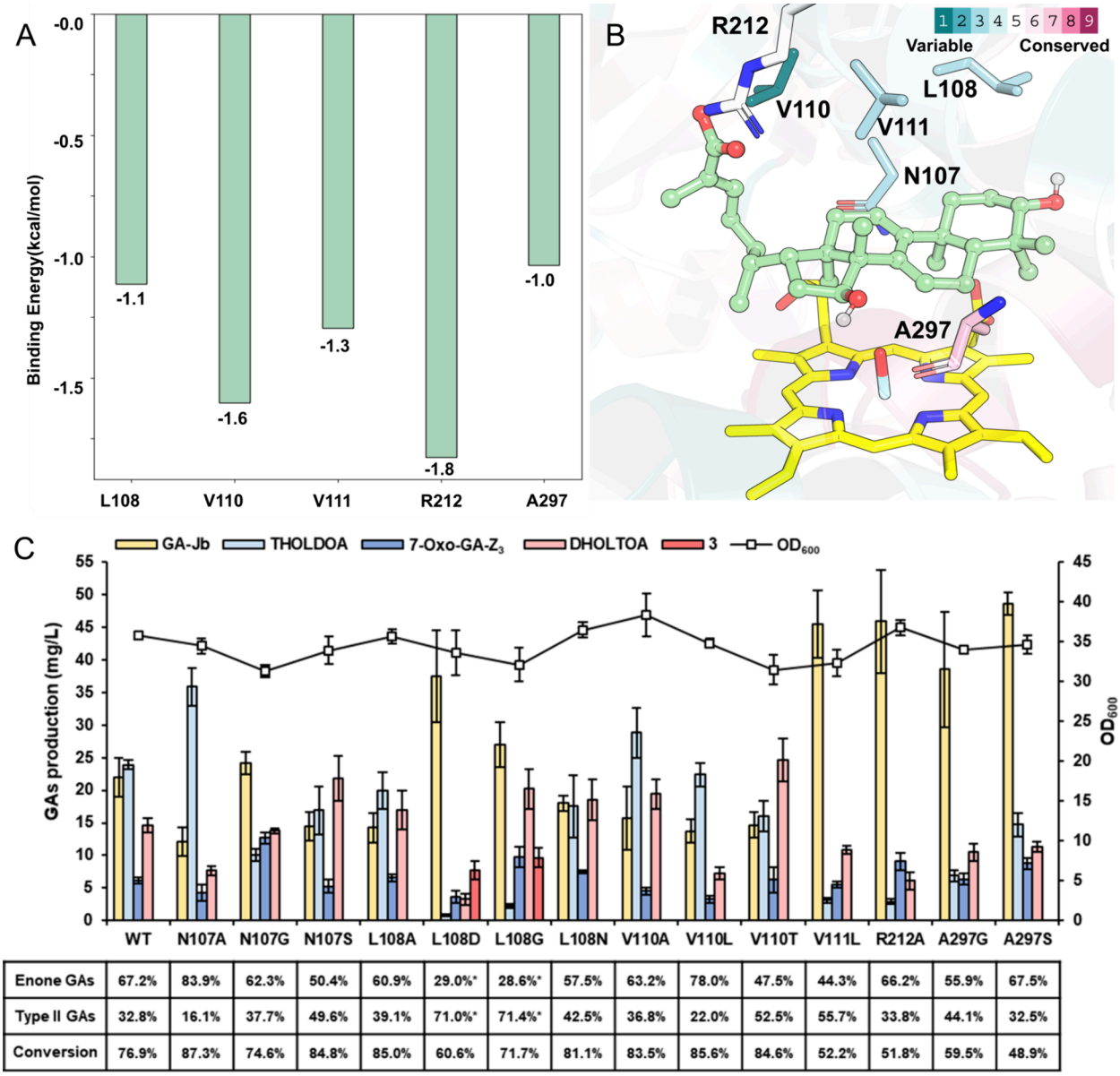

	WT	N107A	N107G	N107S	L108A	L108D	L108G	L108N	V110A	V110L	V110T	V111L	R212A	A297G	A297S
Enone GAs	67.2%	83.9%	62.3%	50.4%	60.9%	29.0%*	28.6%*	57.5%	63.2%	78.0%	47.5%	44.3%	66.2%	55.9%	67.5%
Type II GAs	32.8%	16.1%	37.7%	49.6%	39.1%	71.0%*	71.4%*	42.5%	36.8%	22.0%	52.5%	55.7%	33.8%	44.1%	32.5%
Conversion	76.9%	87.3%	74.6%	84.8%	85.0%	60.6%	71.7%	81.1%	83.5%	85.6%	84.6%	52.2%	51.8%	59.5%	48.9%

Figure 8. Key residues for the substrate specificity and enzyme activity of CYP512A13. (A) Residues that contributed more than 1.0 kcal/mol by energy decomposition. (B) Key residues position in CYP512A13 and their variability in CYP512A13 homologies. (C) Cell growth, GAs production and substrate conversion after 120 h fermentation of CYP512A13 variants. The selectivity refers to the ratio of enone GAs (THOLDOA and 7-oxo-GA-Z_3) or type II GAs (**3** and DHOLTOA) production titers in the total titers of enone GAs and type II GAs. For L108D and L108G, the yield of **3** was estimated using the DHOLTOA standard curve for the selectivity calculation, marked with an asterisk. The conversion refers to the consumed GA-Jb (the difference of the GA-Jb titer by strain SC27-CK and the corresponding variants) to the total titer of GA-Jb (GA-Jb produced by strain SC27-CK). All data represent the mean of four biologically independent samples, and the error bars show the standard deviation.

selectivity, while the production of DHOLTOA revealed C12 and C15 oxidation selectivity. We also noted that peak **3** was detectable in strains SC27-L108D and SC27-L108G (Figure S41). For variants L108D and L108G, the production of **3** and DHOLTOA might reflect the C12 and C15 oxidation selectivities on type II GAs. For the N107A variant, the C7-specific selectivity improved from 67.2% (exhibited by the WT) to 83.9%. This improvement was accompanied by a decrease in the level of production of DHOLTOA (Figure 8C). When N107 was mutated to glycine (G) or serine (S), the corresponding variants exhibited a shift in substrate preference at C15 and C12 as compared to that of N107A. These results suggested that N107 was closely related to substrate selectivity. A similar phenotype was observed at the V110 site. For the V110L variant, the C7-specific selectivity increased from 67.2% (exhibited by the WT) to 78.0%, while the C12- and C15-specific selectivity decreased from 32.8% (exhibited by the WT) to 22.0%. In contrast, the V110T variant altered the C7-specific selectivity to 47.5%, and the C12- and C15-specific selectivity to 52.5%. The variants V111L, R212A, A297G, and A297S converted significantly less GA-Jb than the control strain, indicating that these amino acids were crucial for regulating the overall catalytic activity of CYP512A13. More intriguingly, the L108 site contributed significantly to both catalytic activity and substrate selectivity. Specifically, the substrate conversion decreased from 76.9% (exhibited by the WT) to 60.6% by strain SC27-L108D, and the production of THOLDOA, 7-oxo-GA-Z_3, and DHOLTOA

https://doi.org/10.1021/acscatal.5c04095
ACS Catal. 2025, 15, 13428−13443

was substantially reduced to 0.8, 3.7, and 3.3 mg/L after 120 h of fermentation. However, a small amount of compound **3** accumulated (105.8 mAU·s) (Figure S41). These results suggested that L108D retained the catalytic activity to hydroxylate GA-Jb at C12, but lost most of the catalytic activity required for further oxidizing C15 to form DHOLTOA and for oxidizing GA-Jb at C7 to form 7-oxo-GA-Z_3 and THOLDOA. The mutation of L108 to glycine (G) specifically restored the substrate preference at C12 and C15 to 71.4%, while the substrate preference at C7 in strain SC27-L108N was comparable with that at C12 and C15 (57.5% vs 42.5%).

To understand these changes, we conducted MD simulations on the N107A-GA-Jb complex in the C7 pose and the L108G-GA-Jb complex in the C12 pose. For each model, three independent MD simulations were performed. In N107A, water occupancy was remarkably increased near the C15 hydroxyl in the active pocket. Specifically, the water occupancy within 3 and 5 Å of the oxygen of C15 hydroxyl increased by 153.3 and 483.7%, respectively. The increased water molecules significantly promoted enone formation through water-mediated catalysis (Figure S42). Regarding L108G, the small side chain of L108G enabled the repositioning of GA-Jb, which enlarged the A ($C12-H_R-O$) angle and increased the PRSs for C12 hydroxylation from 6.3 to 16.8%, thereby promoting the formation of type II GAs (Figure S43).

4. DISCUSSION

Renowned as the "immortal mushroom" and a quintessential symbol of traditional Chinese medicine,*G. lucidum*has been therapeutically and prophylactically employed for millennia. Triterpenoids (GAs) derived from them are particularly esteemed for their diverse physiological activities. However, the supply chain relying on mushroom cultivation to produce GAs is fraught with issues, stemming from the undeveloped genetic manipulation of *Ganoderma*, its long growth cycle, and vulnerability to environmental elements such as land, climate, and pests. Synthetic biology-enabled efficient biomanufacturing offers a promising solution to address these issues. In comparison to type II GAs, type I GAs are more abundant and structurally complex, albeit only limited enzymes have been documented.[18,20,21,24] Herein, we disclose a branchpoint CYP that catalyzes the formation of the crucial enone at C7, C8, C9, and C11, thereby enabling interconversion between GA types. Cooperating with other CYPs, CYP512A13 participates in the generation of THOLDOA in the heterologous host, which represents a novel type I GA. In addition, CYP512A13 hydroxylates at C12 and oxidizes at C15 hydroxyl on a type II GA backbone. To our knowledge, no C12 postmodified type II GAs have been previously described. These results exemplify that by circumventing the complex regulation of the native host, synthetic biology can biosynthesize those previously overlooked intermediates or generate novel metabolites.

Currently, various chemical synthetic routes have been established for linear enones.[33] In contrast, chemical synthesis of cyclic enones remains limited, with most reports focusing on monocyclic substrates containing olefinic or phenolic hydroxyl groups.[34,35] To date, successful chemical construction of enones on polycyclic scaffolds has been exclusively documented in abietic acid, a tricyclic diterpenoid featuring an abietane C20 skeleton. Through oxidation of a carbon−carbon conjugated double bond across its B- and C-rings, researchers achieve enone formation with a ketone at the B-ring and a carbon−carbon double bond at the C-ring. Notably, this chemical strategy requires more demanding reaction conditions. Further, the enone yield did not exceed 70% under various conditions, and the target product was susceptible to isomerization or rearrangement.[36,37]

CYPs that catalyze at C7 of steroids or triterpenoids have been reported in several ways.[38−42] Predominantly, there are simple reactions such as hydroxylation or successive oxidations that cannot form an enone. In most instances, when CYP catalyzes the oxidation of a double bond within the ring, it undergoes an epoxidation reaction.[43−45] The epoxy structure in certain compounds is unstable, and backbone rearrangement occurs, resulting in the formation of a carbon−carbon double bond, hydroxyl groups, or other possible changes. Examples include CYP725A4 from *Taxus*[46] and the CYP88A subfamily involved in melianol metabolism, such as CYP88A154 from *Ailanthus altissima*,[47] CYP88A51 from*Citrus sinensis*,[47] and CYP88A108 from*Melia azedarach*.[48] There is also a case where CYP catalyzes the direct oxidation of the double bond on the ring to form a ketone group without proceeding via the epoxy intermediate. For example, CYP7A1 from*Homo sapiens*catalyzes the conversion of 7-dehydrocholesterol to 7-ketocholesterol.[49] The proposed mechanism for the oxidation of 7-dehydrocholesterol to 7-ketocholesterol entails the formation of an $Fe^{III}-O-C-C^{+}$ intermediate, followed by either a 7,8-hydride shift or an alternative ring-closing reaction, ultimately leading to the generation of the epoxide. Previous studies have reported the P450-catalyzed direct oxidation of an olefin to a carbonyl; thus, such a proposed enzymatic mechanism is not unprecedented.[50,51] We report a novel CYP that catalyzes C7 hydrogen abstraction on the conjugated double bond of GA-Jb's B and C rings, leading to enone formation. The unique pocket shape of CYP512A13 properly orients the C7 hydrogen for oxygen activation, enabling efficient hydroxylation. Additionally, the pocket's hydrophilicity and the C15 hydroxyl stabilize a water molecule, which forms a hydrogen bond with the newly generated C7 hydroxyl. This setup lowers the energy requirement to 17.9 kcal/mol for water to extract the C7 hydroxyl hydrogen, converting it to a C7 ketone. Finally, with carboxyl assistance, hydrogen transfers to C11, stabilizing the enone structure. This avoids the high-energy (48.6 kcal/mol) hydrogen transfer from C8 to C9 along the tetracyclic skeleton, making enone formation more feasible.

CYP512A13 mediates the interconversion between different types of GAs, which is accomplished by its substrate selectivity. In our study, we identified two residues (N107 and V110) that are critical for substrate preference shift, three residues (V111, R212, and A297) that are important for the overall catalytic activity, and one residue (L108) that contributes significantly to both catalytic activity and substrate selectivity. For selective oxidation at C7, the best variant N107A achieved 83.9% selectivity with the highest substrate conversion, which was 24.9 and 13.5% higher than those of WT. For selective oxidation at C12 and C15, the best variant L108G achieved 71.4% selectivity, which was 118% higher than that of WT (Figure 8C).

5. CONCLUSIONS

In conclusion, this study uncovers CYP512A13 as a pivotal enzyme for GAs interconversion. It offers valuable insights into the formation mechanism of enone at C7, C8 and C8, C9, thereby enhancing the comprehension, elucidation, and reconstruction of the biosynthetic pathway for type I GAs.

https://doi.org/10.1021/acscatal.5c04095
ACS Catal. 2025, 15, 13428−13443

The variants designed herein can be adopted to achieve the targeted production of different types of GAs. This advancement will significantly expedite the generation of functionalized triterpenoids and their application in medicinal chemistry, food, and other relevant fields.

■ ASSOCIATED CONTENT

Supporting Information

The Supporting Information is available free of charge at https://pubs.acs.org/doi/10.1021/acscatal.5c04095.

Supplementary figures (S1−S43), supplementary tables (S5−S34), scheme for plasmids and strains construction (Table S1), coexpression analysis of *G. lucidum* using RNA sequencing data (Table S2), primers used in this study for CYPs amplification (Table S3), ^{13}C NMR and ^{1}H NMR data of compounds (Table S4), and coordinates of all intermediates and transition states (PDF)

Scheme for plasmid and strain construction (XLSX)

Co-expression analysis of *G. lucidum* using RNA sequencing data (XLSX)

Primers used in this study for CYP amplification (XLSX)

^{13}C-NMR and ^{1}H-NMR data of compounds (XLSX)

MD trajectories indicating the proportions of water molecules within 3 and 5 Å of the C15 hydroxyl oxygen to be 16.5 and 53.3% (MP4)

Coordinates (PDF)

■ AUTHOR INFORMATION

Corresponding Authors

Ting Shi − *State Key Laboratory of Microbial Metabolism, Joint International Research Laboratory of Metabolic & Developmental Sciences, School of Life Sciences and Biotechnology, Shanghai Jiao Tong University, Shanghai 200240, China;* orcid.org/0000-0003-3921-4412; Email: tshi@sjtu.edu.cn

Han Xiao − *State Key Laboratory of Microbial Metabolism, Joint International Research Laboratory of Metabolic & Developmental Sciences, School of Life Sciences and Biotechnology, Shanghai Jiao Tong University, Shanghai 200240, China;* orcid.org/0000-0003-2895-1847; Email: smallhan@sjtu.edu.cn

Authors

Qin Wang − *State Key Laboratory of Microbial Metabolism, Joint International Research Laboratory of Metabolic & Developmental Sciences, School of Life Sciences and Biotechnology, Shanghai Jiao Tong University, Shanghai 200240, China*

Zeqian Du − *State Key Laboratory of Microbial Metabolism, Joint International Research Laboratory of Metabolic & Developmental Sciences, School of Life Sciences and Biotechnology, Shanghai Jiao Tong University, Shanghai 200240, China*

Zhenhao Li − *ShouXianGu Botanical Drug Institute, Hangzhou 311100, China*

Wei Yuan − *Tianjin Institute of Industrial Biotechnology, Chinese Academy of Sciences, Tianjin 300308, China;* orcid.org/0000-0003-4907-8098

Jian-Jiang Zhong − *State Key Laboratory of Microbial Metabolism, Joint International Research Laboratory of Metabolic & Developmental Sciences, School of Life Sciences and Biotechnology, Shanghai Jiao Tong University, Shanghai 200240, China;* orcid.org/0000-0002-2265-9338

Juan Guo − *State Key Laboratory for Quality Ensurance and Sustainable Use of Dao-Di Herbs, National Resource Center for Chinese Materia Medica, China Academy of Chinese Medical Science, Beijing 100700, China; Dalian Institute of Marine Traditional Chinese Medicine, China Academy of Chinese Medical Sciences & Dalian University, Dalian 116622, China;* orcid.org/0000-0002-1327-4428

Shenggan Luo − *State Key Laboratory of Microbial Metabolism, Joint International Research Laboratory of Metabolic & Developmental Sciences, School of Life Sciences and Biotechnology, Shanghai Jiao Tong University, Shanghai 200240, China*

Complete contact information is available at: https://pubs.acs.org/10.1021/acscatal.5c04095

Author Contributions

H.X. and Q.W. conceived and designed the study. H.X., Q.W., and Z.D. wrote the manuscript with partial assistance from T.S., Z.L., J.G., and J.J.Z. Q.W. cultured *Ganoderma* and prepared *G. lucidum* samples for RNA sequencing and metabolite assay. Z.L. analyzed the content of type I GAs of *Ganoderma* samples. Q.W. constructed the CYP expression plasmids, did the screening of CYPs in *S. cerevisiae*, performed the fermentation assay of yeast strains, conducted liter-scale fermentation, purified the compounds, performed the *in vitro* enzymatic assay of CYPs, and analyzed the LC-MS data. W.Y. analyzed the NMR data. Z.D., S.L., and T.S. performed the QM calculation, MD simulation, and other computational analyses. H.X. and T.S. finalized the manuscript. All authors have given approval to the final version of the manuscript. Q.W. and Z.D. contributed equally to this work.

Notes

The authors declare no competing financial interest.

■ ACKNOWLEDGMENTS

This study was supported by the Key Project for Synthetic Biology of Shanghai (24HC2810800 to H.X.), the Key project at central government level: The ability establishment of sustainable use for valuable Chinese medicine resources (2060302-2303-02 to H.X.), Shanghai Municipal Science and Technology Major Project (to T.S.), the National Natural Science Foundation of China (32270038 to T.S.), and Zhejiang Pioneer R&D Program (2025C01133 to Z.L.). We thank Dr. Xudong Qu (Shanghai Jiao Tong University) and Mr. Yinhao Ma (East China Normal University) for their helpful suggestion. The computational simulations in this study were conducted on the π 2.0 cluster, which is supported by the Center for High Performance Computing at Shanghai Jiao Tong University.

■ REFERENCES

(1) Ahmad, M. F.; Wahab, S.; Ahmad, F. A.; Ashraf, S. A.; Abullais, S. S.; Saad, H. H. *Ganoderma lucidum*: a potential pleiotropic approach of ganoderic acids in health reinforcement and factors influencing their production. *Fungal Biol. Rev.* **2022**, *39*, 100−125.

(2) Baby, S.; Johnson, A. J.; Govindan, B. Secondary metabolites from *Ganoderma*. *Phytochemistry* **2015**, *114*, 66−101.

(3) Walker, P. D.; Weir, A. N. M.; Willis, C. L.; Crump, M. P. Polyketide β-branching: diversity, mechanism and selectivity. *Nat. Prod. Rep.* **2021**, *38* (4), 723−756.

(4) Dénès, F.; Farard, J.; Lebreton, J. Synthesis of ^{13}C-labeled steroids. *Synthesis* **2019**, *51* (23), 4311−4337.
(5) Amslinger, S. The tunable functionality of α,β-unsaturated carbonyl compounds enables their differential application in biological systems. *ChemMedChem.* **2010**, *5* (3), 351−356.
(6) Liang, S.; Chen, C.; Chen, R.; Li, R.; Chen, W.; Jiang, G.; Du, L. Michael acceptor molecules in natural products and their mechanism of action. *Front. Pharmacol.* **2022**, *13*, No. 1033003.
(7) Shiraki, T.; Kamiya, N.; Shiki, S.; Kodama, T. S.; Kakizuka, A.; Jingami, H. α,β-Unsaturated ketone is a core moiety of natural ligands for covalent binding to peroxisome proliferator-activated receptor γ. *J. Biol. Chem.* **2005**, *280* (14), 14145−14153.
(8) Dong, T.; Li, C.; Wang, X.; Dian, L.; Zhang, X.; Li, L.; Chen, S.; Cao, R.; Li, L.; Huang, N.; He, S.; Lei, X. Ainsliadimer A selectively inhibits IKKα/β by covalently binding a conserved cysteine. *Nat. Commun.* **2015**, *6* (1), 6522.
(9) Schirmer, A.; Kennedy, J.; Murli, S.; Reid, R.; Santi, D. V. Targeted covalent inactivation of protein kinases by resorcylic acid lactone polyketides. *Proc. Natl. Acad. Sci. U. S. A.* **2006**, *103* (11), 4234−4239.
(10) Widen, J. C.; Kempema, A. M.; Villalta, P. W.; Harki, D. A. Targeting NF-κB p65 with a helenalin inspired bis-electrophile. *ACS Chem. Biol.* **2017**, *12* (1), 102−113.
(11) Honda, T.; Rounds, B. V.; Bore, L.; Finlay, H. J.; Favaloro, F. G.; Suh, N.; Wang, Y.; Sporn, M. B.; Gribble, G. W. Synthetic oleanane and ursane triterpenoids with modified rings A and C: a series of highly active inhibitors of nitric oxide production in mouse macrophages. *J. Med. Chem.* **2000**, *43* (22), 4233−4246.
(12) Li, X.; Zuo, Y.; Tang, G.; Wang, Y.; Zhou, Y.; Wang, X.; Guo, T.; Xia, M.; Ding, N.; Pan, Z. Discovery of a series of 2,5-diaminopyrimidine covalent irreversible inhibitors of Bruton's tyrosine kinase with in vivo antitumor activity. *J. Med. Chem.* **2014**, *57* (12), 5112−5128.
(13) Chen, X.; Zhao, J.; Chen, L.; Wang, S.; Wang, Y.; Li, S. Lanostane triterpenes from the mushroom *Ganoderma resinaceum* and their inhibitory activities against α-glucosidase. *Phytochemistry* **2018**, *149*, 103−115.
(14) Kou, R.; Xia, B.; Wang, Z.; Li, J.; Yang, J.; Gao, Y.; Yin, X.; Gao, J. Triterpenoids and meroterpenoids from the edible *Ganoderma resinaceum* and their potential anti-inflammatory, antioxidant and anti-apoptosis activities. *Bioorg. Chem.* **2022**, *121*, No. 105689.
(15) Wu, T.; Shi, L.; Kuo, S. Cytotoxicity of *Ganoderma lucidum* triterpenes. *J. Nat. Prod.* **2001**, *64* (8), 1121−1122.
(16) Cheng, C.; Yue, Q.; Wu, Z.; Song, X.; Tao, S.; Wu, X.; Xu, P.; Liu, X.; Guan, S.; Guo, D. Cytotoxic triterpenoids from *Ganoderma lucidum*. *Phytochemistry* **2010**, *71* (13), 1579−1585.
(17) Liang, C.; Tian, D.; Liu, Y.; Li, H.; Zhu, J.; Li, M.; Xin, M.; Xia, J. Review of the molecular mechanisms of *Ganoderma lucidum* triterpenoids: Ganoderic acids A, C2, D, F, DM, X and Y. *Eur. J. Med. Chem.* **2019**, *174*, 130−141.
(18) Yuan, W.; Jiang, C.; Wang, Q.; Fang, Y.; Wang, J.; Wang, M.; Xiao, H. Biosynthesis of mushroom-derived type II ganoderic acids by engineered yeast. *Nat. Commun.* **2022**, *13* (1), 7740.
(19) Wang, Q.; Li, Y.; Zhang, S.; Yuan, W.; Du, Z.; Shi, T.; Chang, Z.; Zhai, X.; Lu, Y.; Wang, M.; Guo, J.; Zhong, J.; Xiao, H. Decoding and reprogramming of the biosynthetic networks of mushroom derived bioactive type II ganoderic acids in yeast. *Cell Discovery* **2025**, *11*, 61.
(20) Yang, C.; Li, W.; Li, C.; Zhou, Z.; Xiao, Y.; Yan, X. Metabolism of ganoderic acids by a *Ganoderma lucidum* cytochrome P450 and the 3-keto sterol reductase ERG27 from yeast. *Phytochemistry* **2018**, *155*, 83−92.
(21) Wang, W.; Xiao, H.; Zhong, J. Biosynthesis of a novel ganoderic acid by expressing CYP genes from *Ganoderma lucidum* in *Saccharomyces cerevisiae*. *Appl. Microbiol. Biotechnol.* **2022**, *106* (2), 523−534.
(22) Hirotani, M.; Asaka, I.; Furuya, T. Investigation of the biosynthesis of 3α-hydroxy triterpenoids, ganoderic acids T and S, by application of a feeding experiment using [1, 2-$^{13}C_2$] acetate. *J. Chem. Soc., Perkin Trans.* **1990**, *10*, 2751−2754.
(23) Chen, S.; Xu, J.; Liu, C.; Zhu, Y.; Nelson, D. R.; Zhou, S.; Li, C.; Wang, L.; Guo, X.; Sun, Y.; Luo, H.; Li, Y.; Song, J.; Henrissat, B.; Levasseur, A.; Qian, J.; Li, J.; Luo, X.; Shi, L.; He, L.; Xiang, L.; Xu, X.; Niu, Y.; Li, Q.; Han, M. V.; Yan, H.; Zhang, J.; Chen, H.; Lv, A.; Wang, Z.; Liu, M.; Schwartz, D. C.; Sun, C. Genome sequence of the model medicinal mushroom *Ganoderma lucidum*. *Nat. Commun.* **2012**, *3* (1), 913.
(24) Wang, W.; Xiao, H.; Zhong, J. Biosynthesis of a ganoderic acid in *Saccharomyces cerevisiae* by expressing a cytochrome P450 gene from *Ganoderma lucidum*. *Biotechnol. Bioeng.* **2018**, *115* (7), 1842−1854.
(25) Galappaththi, M. C. A.; Patabendige, N. M.; Premarathne, B. M.; Hapuarachchi, K. K.; Tibpromma, S.; Dai, D.; Suwannarach, N.; Rapior, S.; Karunarathna, S. C. A review of *Ganoderma* triterpenoids and their bioactivities. *Biomolecules* **2023**, *13*, 24.
(26) Fang, Q.; Zhong, J. Two-stage culture process for improved production of ganoderic acid by liquid fermentation of higher fungus *Ganoderma lucidum*. *Biotechnol. Prog.* **2002**, *18* (1), 51−54.
(27) Xu, Y.; Zhong, J. Impacts of calcium signal transduction on the fermentation production of antitumor ganoderic acids by medicinal mushroom *Ganoderma lucidum*. *Biotechnol. Adv.* **2012**, *30* (6), 1301−1308.
(28) Gietz, R. D.; Schiestl, R. H. High-efficiency yeast transformation using the LiAc/SS carrier DNA/PEG method. *Nat. Protoc.* **2007**, *2* (1), 31−34.
(29) Shahrokh, K.; Orendt, A.; Yost, G. S.; Cheatham, T. E., III Quantum mechanically derived AMBER-compatible heme parameters for various states of the cytochrome P450 catalytic cycle. *J. Comput. Chem.* **2012**, *33* (2), 119−133.
(30) Case, D.; Ben Shalom, I.; Brozell, S. R.; Cerutti, D. S.; Cheatham, T.; Cruzeiro, V. W. D.; Darden, T.; Duke, R.; Ghoreishi, D.; Gilson, M.; Gohlke, H.; Götz, A.; Greene, D.; Harris, R.; Homeyer, N.; Huang, Y.; Izadi, S.; Kovalenko, A.; Kurtzman, T.; Kollman, P. A. *Amber 2018*; University of California: San Francisco, 2018.
(31) *Gaussian 16 Rev. B.01*; Gaussian, Inc.: Wallingford, CT, 2016.
(32) Luo, Y.; Du, Z.; Jiang, C.; Yu, Z.; Zhong, J.; Shi, T.; Xiao, H. Rational engineering of a membrane-anchored promiscuous cytochrome P450 for the efficient biosynthesis of valuable ganoderic acids. *ACS Catal.* **2023**, *13* (24), 15673−15681.
(33) Zhang, S.; Neumann, H.; Beller, M. Synthesis of α,β-unsaturated carbonyl compounds by carbonylation reactions. *Chem. Soc. Rev.* **2020**, *49* (10), 3187−3210.
(34) Catino, A. J.; Forslund, R. E.; Doyle, M. P. Dirhodium(II) caprolactamate: an exceptional catalyst for allylic oxidation. *J. Am. Chem. Soc.* **2004**, *126* (42), 13622−13623.
(35) Dohi, T.; Nakae, T.; Takenaga, N.; Uchiyama, T.; Fukushima, K.; Fujioka, H.; Kita, Y. μ-Oxo-bridged hypervalent Iodine(III) compound as an extreme oxidant for aqueous oxidations. *Synthesis* **2012**, *44* (08), 1183−1189.
(36) Masnyk, M.; Butkiewicz, A.; Górecki, M.; Luboradzki, R.; Paluch, P.; Potrzebowski, M. J.; Frelek, J. In depth analysis of chiroptical properties of enones derived from abietic acid. *J. Org. Chem.* **2018**, *83* (7), 3547−3561.
(37) Masnyk, M.; Kuśmirek, D.; Trzybiński, D.; Frelek, J. Research into the oxidation of abietic acid−derived enone with atmospheric oxygen. *Chirality* **2020**, *32* (4), 437−445.
(38) Cao, Z. Q.; Lv, J. M.; Liu, Q.; Qin, S. Y.; Chen, G. D.; Dai, P.; Zhong, Y.; Gao, H.; Yao, X. S.; Hu, D. Biosynthetic study of cephalosporin P1 reveals a multifunctional P450 enzyme and a site-selective acetyltransferase. *ACS Chem. Biol.* **2020**, *15* (1), 44−51.
(39) Lv, J. M.; Hu, D.; Gao, H.; Kushiro, T.; Awakawa, T.; Chen, G. D.; Wang, C. X.; Abe, I.; Yao, X. S. Biosynthesis of helvolic acid and identification of an unusual C-4-demethylation process distinct from sterol biosynthesis. *Nat. Commun.* **2017**, *8* (1), 1644.

https://doi.org/10.1021/acscatal.5c04095
ACS Catal. 2025, 15, 13428−13443

(40) Schmitz, D.; Zapp, J.; Bernhardt, R. Steroid conversion with CYP106A2−production of pharmaceutically interesting DHEA metabolites. *Microb. Cell Fact.* **2014**, *13* (1), 81.
(41) Takase, S.; Kera, K.; Nagashima, Y.; Mannen, K.; Hosouchi, T.; Shinpo, S.; Kawashima, M.; Kotake, Y.; Yamada, H.; Saga, Y.; Otaka, J.; Araya, H.; Kotera, M.; Suzuki, H.; Kushiro, T. Allylic hydroxylation of triterpenoids by a plant cytochrome P450 triggers key chemical transformations that produce a variety of bitter compounds. *J. Biol. Chem.* **2019**, *294* (49), 18662−18673.
(42) Russell, D. W. The enzymes, regulation, and genetics of bile acid synthesis. *Annu. Rev. Biochem.* **2003**, *72*, 137−174.
(43) Yan, Y.; Liu, Q.; Zang, X.; Yuan, S.; Bat-Erdene, U.; Nguyen, C.; Gan, J.; Zhou, J.; Jacobsen, S. E.; Tang, Y. Resistance-gene-directed discovery of a natural-product herbicide with a new mode of action. *Nature* **2018**, *559* (7714), 415−418.
(44) Geisler, K.; Hughes, R. K.; Sainsbury, F.; Lomonossoff, G. P.; Rejzek, M.; Fairhurst, S.; Olsen, C.-E.; Motawia, M. S.; Melton, R. E.; Hemmings, A. M.; Bak, S.; Osbourn, A. Biochemical analysis of a multifunctional cytochrome P450 (CYP51) enzyme required for synthesis of antimicrobial triterpenes in plants. *Proc. Natl. Acad. Sci. U. S. A.* **2013**, *110* (35), E3360−E3367.
(45) Miettinen, K.; Pollier, J.; Buyst, D.; Arendt, P.; Csuk, R.; Sommerwerk, S.; Moses, T.; Mertens, J.; Sonawane, P. D.; Pauwels, L.; Aharoni, A.; Martins, J.; Nelson, D. R.; Goossens, A. The ancient CYP716 family is a major contributor to the diversification of eudicot triterpenoid biosynthesis. *Nat. Commun.* **2017**, *8* (1), 14153.
(46) Zhao, Y.; Liang, F.; Xie, Y.; Duan, Y.-T.; Andeadelli, A.; Pateraki, I.; Makris, A. M.; Pomorski, T. G.; Staerk, D.; Kampranis, S. C. Oxetane ring formation in taxol biosynthesis is catalyzed by a bifunctional cytochrome P450 enzyme. *J. Am. Chem. Soc.* **2024**, *146* (1), 801−810.
(47) De La Peña, R.; Hodgson, H.; Liu, J. C. T.; Stephenson, M. J.; Martin, A. C.; Owen, C.; Harkess, A.; Leebens-Mack, J.; Jimenez, L. E.; Osbourn, A.; Sattely, E. S. Complex scaffold remodeling in plant triterpene biosynthesis. *Science* **2023**, *379* (6630), 361−368.
(48) Chuang, L.; Liu, S.; Franke, J. Post-cyclization skeletal rearrangements in plant triterpenoid biosynthesis by a pair of branchpoint isomerases. *J. Am. Chem. Soc.* **2023**, *145* (9), 5083−5091.
(49) Shinkyo, R.; Xu, L.; Tallman, K. A.; Cheng, Q.; Porter, N. A.; Guengerich, F. P. Conversion of 7-dehydrocholesterol to 7-Ketocholesterol Is catalyzed by human cytochrome P450 7A1 and occurs by direct oxidation without an epoxide Intermediate. *J. Biol. Chem.* **2011**, *286* (38), 33021−33028.
(50) Liebler, D. C.; Guengerich, F. P. Olefin oxidation by cytochrome P-450: evidence for group migration in catalytic intermediates formed with vinylidene chloride and trans-1-phenyl-1-butene. *Biochemistry* **1983**, *22* (24), 5482−5489.
(51) Mansuy, D.; Leclaire, J.; Fontecave, M.; Momenteau, M. Oxidation of monosubstituted olefins by cytochromes P-450 and heme models: Evidence for the formation of aldehydes in addition to epoxides and allylic alcohols. *Biochem. Biophys. Res. Commun.* **1984**, *119* (1), 319−325.

https://doi.org/10.1021/acscatal.5c04095
ACS Catal. 2025, 15, 13428−13443